Mechanisms controlling albite dissolution/precipitation kinetics as a function of chemical affinity: New insights from experiments in 29Si spiked solutions at 150 and 180 °C

Jacques Schott, Giuseppe D. Saldi, Chen Zhu, Lei Gong, Kaiyun Chen

Mechanisms controlling albite dissolution/precipitation kinetics as a function of chemical affinity: New insights from experiments in ^{29}Si spiked solutions at 150 and 180 °C

Jacques Schott [a], Giuseppe D. Saldi [a,b,*], Chen Zhu [c], Lei Gong [c], Kaiyun Chen [d]

[a] *Geosciences Environnement Toulouse (GET), Observatoire Midi-Pyrénées, Université de Toulouse, CNRS, IRD, UPS, 14 Avenue Edouard Belin, 31400 Toulouse, France*
[b] *Dipartimento di Fisica e Geologia, Università di Perugia,via Pascoli 35, 06123 Perugia, Italia*
[c] *Department of Earth and Atmospheric Sciences, Indiana University, Bloomington, IN 47405, USA*
[d] *State Key Laboratory of Continental Dynamics, Department of Geology, Northwest University, Xi'an 710069, China*

* Corresponding author
E-mail address: giuseppe.saldi@unipg.it

ABSTRACT

Knowledge of the rates of dissolution of rock-forming minerals close to equilibrium and their dependence on ΔG_r, the Gibbs free energy of reaction, is essential for describing the temporal and spatial evolution of many environmental and engineering processes involving solid/fluid interactions. In the present study we used the isotope-doping method to quantify albite forward and net dissolution rates. Batch experiments were performed at 150, 180°C and pH = 9 at near equilibrium and equilibrium conditions (-25 ≤ ΔG_r ≤ + 8.2 kJ/mol) in ^{29}Si spiked solutions which were undersaturated with the secondary Al-Si solid phases likely to precipitate.

The forward dissolution rates normalized to the initial BET surface area were found to decrease continuously and monotonically with increasing time and ΔG_r, achieving values 1.3 to 2.4 orders of magnitude lower at chemical equilibrium than initial far from equilibrium values, with the highest rate decrease for the highest solid to fluid ratio. These rate drops were accompanied by an increase in BET specific surface areas associated with the formation of widespread dissolution features. A decrease of albite forward dissolution rate together with an increase of its BET surface area was also observed as a function of reaction time at far from equilibrium conditions (ΔG_r ≤ - 65 kJ/mol). These observations are consistent with a continuous decrease with time and increasing ΔG_r of albite effective surface area linked to the formation of unreactive negative crystal facets, in addition to etch pits stopping nucleating above a critical value of ΔG_r. Thus, the observed decrease in albite dissolution rate as equilibrium is approached is not linked primarily to the increase in the contribution of the backward reaction but rather to the decrease of the forward reaction rate in conjunction with the decrease in the density of reactive sites at the mineral surface.

The results of this study show that the characterization of the effective surface area and its evolution with reaction time and chemical affinity is crucial to deriving robust dissolution rates of well-crystallized minerals like feldspars. Dissolution experiments in ^{29}Si spiked solutions of samples with different history and well-characterized effective surface area and surface morphology should help to better quantify the rate laws controlling silicate minerals weathering.

Keywords: Albite dissolution/precipitation kinetics; Gibbs free energy; reactive surface area; Silicon isotopes; Transition State Theory

1. INTRODUCTION

Knowledge of rock-forming silicate minerals reaction rates and mechanisms in natural environments from the critical zone to the deeper crust is essential for quantifying mass transfers at the Earth's surface and their impact on climate, as well in engineered water-rock systems such as geothermal energy or mineral sequestration of CO_2. Among silicate minerals feldspars are of particular interest because their weathering exerts a major control on the formation of clay minerals and the chemistry of natural waters. As a result, feldspars dissolution kinetics has been studied extensively in the last decades resulting in the generation of a substantial database of dissolution rate constants covering a large range of temperatures and fluid pH (e. g. Palandri and Kharaka, 2004; Bandstra et al., 2008; Heřmanská et al., 2022). Most of these data, derived from flow-through experiments and changes in solution chemistry (mostly Si concentrations), were obtained far from thermodynamic equilibrium due in part to the difficulty of rigorously quantifying the departure from equilibrium and the small aqueous concentration changes induced by near-equilibrium feldspar dissolution or precipitation. However, most alkali feldspar-fluid interactions occurring in natural environments, especially in the case of albite, proceed close to equilibrium, as demonstrated by the close to one saturation state of many natural waters with respect to albite (Stefánsson et al., 2001) and the ubiquitous observation of albite local equilibrium weathering regime in field systems (Navarre-Sitchler & Brantley, 2007; Lebedeva et al., 2010).

The principle of detailed balancing at equilibrium has been often used to extrapolate the far-from-equilibrium alkali feldspars rate data to near-equilibrium conditions. It states that the overall rate of any elementary reversible reaction (r_{net}) can be separated into the contributions from the forward (r_+) and backward (r_-) rates and can be related to the reaction Gibbs free energy according to:

$$r_{net} = r_+ - r_- = r_+\left(1 - e^{\Delta G_r/RT}\right). \quad (1)$$

This type of laws, including those taking into account inhibitory/catalytic effects of various aqueous species, have been incorporated in reactive transport codes to model chemical weathering at different spatio-temporal scales (e. g., Lasaga et al., 1994; Goddéris et al., 2006, 2010; Maher et al., 2009). A handful of experiments have measured albite and K-feldspar dissolution rates over a range of Gibbs free energy values approaching equilibrium conditions (e.g., Burch et al., 1993; Gautier et al., 1994; Oelkers et al., 1994; Beig and Lüttge, 2006; Hellmann and Tisserand, 2006; Arvidson and Lüttge, 2010; Pollet-Villard et al., 2016a). Comparison of the data collected by different investigators generally reveal fundamental differences in the dependence of dissolution rates on the distance from

equilibrium. Gautier et al. (1994) and Oelkers et al. (1994), for instance, observed a simple dependence of rates on ΔG_r similar to that described by Eq. (1), whereas Burch et al. (1993) and Hellmann & Tisserand (2006) reported a highly non-linear, sigmoidal dependence characterized by a sharp decrease of dissolution rates below a critical value of ΔG_r. The latter authors explained this sigmoidal behavior by dissolution controlled by two parallel reactions: far from equilibrium it is driven by the nucleation at dislocation outcrops of etch pits that are the source for steps travelling across the crystal surface (Lasaga and Lüttge, 2001); closer to equilibrium, above a critical ΔG_r value, etch pits stop nucleating and dissolution occurs only at pre-existing edges and corners at a much slower pace (cf. Arvidson and Lüttge, 2010).

However, several obstacles make it difficult to compare and interpret the results of available experiments on feldspar dissolution rate as a function of distance to equilibrium.

a) There is a general agreement that mineral dissolution proceeds via parallel reactions occurring at 'active sites' of the crystal surface, which consist of dislocations, edges, microfractures, point defects, steps and kinks, twin boundaries, etc. (Schott et al., 1989; Lasaga and Lüttge, 2001; Higgins et al., 2002; Arvidson and Lüttge, 2010; Pollet-Villard et al., 2016b). This concept of selective dissolution at specific sites raises several difficulties for characterizing i) the effective surface area required for normalizing dissolution rates, ii) the contribution of the different active sites to dissolution as a function of the chemical affinity of the overall dissolution reaction, and for comparing the dissolution rates of natural samples that could exhibit an enormous range of various defects densities.

b) The accurate calculation of the distance to equilibrium in experimental runs is a major challenge because there are significant uncertainties in the literature values of feldspars thermodynamic parameters – for example there is a difference of 4 kJ/mol between the values of albite Gibbs free energy at 25°C reported by Helgeson et al. (1978) and Holland and Powell (2011) – and because quantification of the actual activity of $Al^{3+}_{(aq)}$ or $Al(OH)^{4-}_{(aq)}$ is difficult. As a result, experimental runs where chemical affinity values have not been derived from independent determination of the solubility product of the feldspar used in these runs may be affected by large uncertainties, especially for $|\Delta G_r| < 10$ kJ/mol.

c) Feldspars close-to-equilibrium dissolution/precipitation rates could be extremely slow and, thus, their accurate determination and break down in terms of forward and backward rates may be very difficult. To overcome this difficulty, recent studies have applied Si isotope spiking methods to

decouple forward and backward reactions and quantify the forward dissolution and backward precipitation rates of quartz and feldspar at equilibrium and near equilibrium conditions (Liu et al., 2016; Gruber et al., 2014; Zhu et al., 2016). This method allows a mineral sample containing the naturally abundant ^{28}Si isotope to react in a solution enriched with the rare ^{29}Si isotope. Dissolution and precipitation reactions of the reacting mineral can be decoupled because, whereas mineral dissolution leads to an enrichment of the fluid in ^{28}Si, its precipitation does not noticeably change the isotopic ratios of the fluid (the fractionation effect during precipitation in a heavily spiked fluid is negligible). However, in the case of feldspars it proved difficult to perform near-equilibrium runs while avoiding the precipitation of secondary phases (gibbsite, imogolite, kaolinite; see Zhu et al., 2020) and thus to distinguish via the measurement of the $^{28}Si/^{29}Si$ ratio the precipitation of feldspar from that of secondary clays. Only runs performed at pH(T) ~ 9 and T ≥ 150°C appear to prevent noticeable amounts of secondary phases to precipitate at near equilibrium conditions (Oelkers et al., 1994; Gautier et al., 1994; Hellmann and Tisserand, 2006).

The goal of the present study is to improve our knowledge of the mechanisms that control albite dissolution and precipitation kinetics near thermodynamic equilibrium and thus our ability to describe the weathering rates of this mineral in natural processes. Towards this goal, we performed albite dissolution and precipitation experiments with and without ^{29}Si tracer at 150 and 180°C and pH 9 as a function of the distance from equilibrium. The experiments with the isotope tracer were conducted in batch reactors in solutions strongly undersaturated with respect to albite and were let run enough time after the attainment of albite equilibrium to determine this mineral solubility product. Albite precipitation kinetics was analyzed within the framework of relaxation kinetics in a run where a solution in equilibrium with albite at 180°C was quickly cooled to 150°C and let relax to a new equilibrium at this temperature. Albite dissolution experiments without ^{29}Si isotope tracer were performed at 150°C, pH = 9 and far from equilibrium conditions (ΔG_r < - 60 kJ/mol) to accurately quantify the dissolution rate constant of this mineral.

2. MATERIALS AND METHODS

2.1 Albite grains preparation and characterization

Research grade albite crystals (from Bancroft, Ontario, Canada) were purchased from Ward's Natural Sciences Establishment, Inc. The crystals were handpicked, ground with a with a ball mill, and

subsequently dry-sieved through a clean copper mesh to retain the 53-106 µm size fraction. There were many submicron-to-micron particles that adhered to the surface of these freshly ground grains. The dissolution of these ultra-fine particles may result in initially nonlinear rates of reaction or parabolic kinetics (Holdren and Berner, 1979; Schott et al., 1981; Lu et al., 2013). To remove these particles, the ground feldspar grains were ultrasonically cleaned with deionized water and ethanol eight times for about 5 minutes per treatment. The cleaned albite grains were then dried overnight in an oven at 50 °C and subsequently kept in a desiccator. Scanning Electron Microscopy (SEM) photomicrographs of albite surface after ultrasonic cleaning can be seen in Fig. 1. Only few fine particles can be seen on the mineral surfaces.

The purity of the albite crystals was examined with powder X-ray diffraction (XRD), using a Bruker D8 Advance diffractometer, equipped with a Cu anode at 20 kV and 5 mA, and with a SolX energy-dispersive detector. The scan parameters used were 2 to 70° 2ϑ, with a step size of 0.02°2ϑ. Starting samples were ground by hand in an agate mortar and pestle to get sufficiently small particles. These particles were subsequently filled into a titanium sample holder for XRD analysis. The resulting XRD pattern is reported in Fig. 2 and corresponds to an ordered albite with small amounts of anorthite (6.4 % wt) and microcline (6.1 % wt), without any other phase detectable.

Scanning Electron Microscopy (SEM) observations of initial non-reacted and reacted albite grains were performed at the Raimond Castaing Center in Toulouse using a JEOL JSM 7800F coupled with energy dispersive X-ray (EDX) spectroscopy.

The specific surface area (SSA) of the clean albite powder was measured by 11-point Kr adsorption analyses according to the BET method using a Quantachrome Autosorb-1. The specific surface area was found to be equal 0.135 ± 0.005 $m^2.g^{-1}$**.** The albite Si isotope composition is reported in Table 1.

2.2 ^{29}Si stock solution for isotope tracer experiments

Except where noted, all chemicals used were analytical grade. In order to prepare the ^{29}Si stock solution, $^{29}SiO_2$ enriched powder (with isotope abundance of 0.0004 ^{28}Si, 0.9990 ^{29}Si, and 0.0006 ^{30}Si from Isoflex, San Francisco, CA, USA) were dissolved by alkali flux (Georg et al., 2006). Briefly, 0.0488 (± 0.001) g of $^{29}SiO_2$ powder and 0.4880 (± 0.001) g of NaOH were placed in a silver crucible that was subsequently put into a 730 °C preheated muffle furnace and held for 10 minutes. After cooling to room temperature, the mixture was dissolved in 500 ml ultrapure water (18.2 MΩ, Millipore) and the solution was then transferred into a clean 500 ml polypropylene bottle. Then, the solution (i.e., 1.6

mM $^{29}SiO_2$) was poured into a vacuum filter system (Thermo Scientific, Nalgene, sterile analytical filter) which used a piece of 0.22 µm nitrocellulose membrane filter paper (Fisher Scientific, Pittsburgh, PA, USA). The filtered stock solution was collected into a new, clean 500 ml polypropylene bottle and stored in a refrigerator at 4.0 °C.

2.3 Experimental conditions of dissolution and precipitation experiments with isotope tracer

Albite dissolution/precipitation experiments were performed in a 450 mL titanium batch reactor at temperatures of 150 and 180°C and at N_2 partial pressure of 15 bar. The solid suspension in the reactor was stirred at a constant rate with a Parr magnetically driven stirrer and kept at a constant temperature (±1°C) by a Parr controlled furnace. Fluid samples were taken at predetermined times during each run to follow the chemical and isotopic evolution of the solution and to check the achievement of chemical equilibrium between solid and solution. The samples were taken via a stainless steel valve and a titanium dip-tube equipped at its end with a 10 µm titanium frit immersed in the solution. Before flowing through the sampling valve, the collected fluid was cooled with cold water via a cooling sleeve mounted along the outer portion of the sampling tube. For each sample about 10 mL of solution were withdrawn and filtered using PTFE syringe filters with 0.20 µm pore size, whereas the first two ml collected were discarded. Duplicate aliquots were acidified using ultrapure HNO_3 65% for subsequent measurements of Si, Al and Na concentrations, and Si isotopes composition. Non-acidified aliquots were used for pH measurements, which were performed immediately after sampling.

In addition, to unambiguously determine albite dissolution rate constant k_+ at 150°C and pH= 9, three albite dissolution runs were performed without isotope tracer at far from equilibrium conditions ($-64 \leq \Delta G_r \leq -28$ kJ/mol) using a 300 ml mixed-flow Ti-reactor (see its description in Gautier et al., 2001).

The albite precipitation run was performed by perturbing the chemical equilibrium by a sudden change in temperature and letting the system relax to a new equilibrium. Resulting precipitation data can be analyzed using the relaxation kinetics approach (see § 2.8). In practice, after reaching the chemical equilibrium during the dissolution of albite at 180°C, the temperature was decreased to 150°C, resulting in the fluid becoming supersaturated with respect to albite ($\Omega \sim 10$), and provoking precipitation until new chemical equilibrium was attained.

The initial solution was prepared by adding ~ 1.5 ml of the $^{29}SiO_2$ stock solution to 40 ml of ultra-high purity water pre-equilibrated with SiO_2 (Si = 67mg.L^{-1}) and a small amount of NaOH 1 M to obtain a solution pH value of 11.6 (~ 9.2 at 150°C) for a final solution volume of 500 ml. The initial solution mass used for the experiments at 150 and 180 °C, was ~ 427 and 409 g, respectively. The initial concentrations of each constituent, the ^{29}Si initial abundance and the mass of albite and aqueous solution used for each experiment are listed in Table 1.

The list of the experiments conducted at far-from-equilibrium conditions using a mixed-flow reactor is reported in Table 2 with the corresponding experimental parameters.

2.4 Sample pre-treatment before isotopic analysis

To reduce the interferences from other cations when measuring silicon isotope, all solution samples were purified by cation exchange chromatography. Details about the chemical procedure are described in Georg et al. (2006). Briefly, 1.8 ml Bio-Rad AG 50W-X8 resin was placed in a 10-ml Poly-Prep chromatography column. The resin was rinsed with hydrochloric acid and DI water as follows: 6.0 ml DI water, 6.0 ml 3.0N HCl, 6.0 ml 6.0N HCl, 4.0 ml 37% HCl, 6.0 ml 6.0N HCl, 10 ml 3.0N HCl, and thrice 5.0 ml DI water. Then 1.0 ml solution sample was added to the column to condition the resin. Afterward, 7.0 ml of the solution sample was loaded onto the column and the filtered solution was collected in a clean polystyrene 15-ml conical centrifuge tube (Fisher Scientific, Pittsburgh, PA, USA) in preparation for isotope analysis.

2.5 Measurements of silicon stable isotopes

The Si isotope ratios were measured using high-resolution multiple-collector inductively coupled plasma mass spectrometry (HR-MC-ICP-MS, Nu Plasma II, Wrexham, UK) at Northwest University, China. Blank samples were filled with ultrapure DI water and acidified with ultrapure HNO_3. The Si isotope ratios were measured using Faraday cups under static mode. Instrumental sensitivity was ~11V μg^{-1} g^{-1} for ^{28}Si in high-resolution mode. The fractions of ^{28}Si, ^{29}Si, and ^{30}Si were calculated by the measured $^{28}Si/^{29}Si$ and $^{28}Si/^{30}Si$ ratios. The sample solution was introduced into the MC-ICP-MS using a dry aerosol system (Aridus II, Cetac, USA) and a 100 µl min^{-1} PFA micro-flow nebulizer. Sample standard bracketing (SSB, Alfa Aesar Si, Stock# 38717, LOT 591543G) was adopted to calibrate the instrument isotopic bias. The isotopic abundance of every sample was determined by averaging the three duplicate measurements using the Time-Resolved-Analysis (TRA) method. The relative standard

deviation (RSD) of the three ratios was used to evaluate the data quality. Only those analyses with RSD ($\delta^{30}Si$) <10% were reported; samples with RSD ($\delta^{30}Si$) >10 % were re-measured.

2.6 Determination of metals aqueous concentrations and pH

The concentrations of Na, Al and Si were determined using inductively coupled plasma optical emission spectroscopy (ICP-OES, Horiba Ultima 2). All measurements were carried out in triplicates on samples diluted in an aqueous 2% HNO_3 solution. Uncertainties were estimated from repeated measurements to be < 2 %. Detection limits were 0.9, 0.45 and 0.71 µmol/kg for Na, Al and Si, respectively. Fluid pH was determined just after sampling using a Metrohm pH microelectrode calibrated against NIST certified buffers (pH = 4.0, 7.00 and 10.01 at 25 °C).

2.7 Thermodynamic calculations.

Based on the measured concentrations of Si, Al, and Na and pH, the speciation of the aqueous solutions and their saturation state with respect to albite were calculated using the PHREEQC v3.6.2 software (Parkhurst and Appelo, 2013) with the Carbfix database (Voigt et al., 2018). This database includes internally consistent stability constants of aqueous Al species allowing a robust evaluation of the saturation state (Ω) of the fluid with respect to albite and the chemical affinity ($A = -\Delta G_r$) of albite dissolution reaction:

$$NaAlSi_3O_8 + H_2O = Na^+ + Al(OH)_4^- + 3SiO_2(aq)\ . \qquad (2)$$

The thermodynamic properties of albite differ significantly due to compositional and structural variations (Arnórsson and Stefánsson, 1999). Using the value of the albite solubility product (log K_{sp}(25 °C) = -20.12) provided by the Carbfix database, which was derived from Helgeson et al. (1978), and the corresponding analytical expression employed by PHREEQC to calculate its temperature variation, would result in values of $\Omega \leq 0.1$ at steady-state conditions. We thus followed the approach of Gautier et al. (1994), and, as in our experiments albite long-term (> 30 days) dissolution at 150 and 180°C led to constant compositions of the solution and values of albite ion activity product (IAP), we assumed that these steady-state values of albite IAP correspond to the albite solubility product, K_{sp}, (Ω = 1). These values were incorporated in the Carbfix thermodynamic database in place of the values deduced from Helgeson et al., 1978 (see § 3.2).

2.8 Analysis of albite dissolution/precipitation rate data

Experimental data on mineral dissolution and growth rates are often analyzed using the following general rate equation (Aagard and Helgeson, 1982; Lasaga, 1998):

$$r_{net} = k_0 S_e exp^{\frac{E_a}{RT}} a_{H^+,OH^-}^{n_{H^+,OH^-}} g(I) \prod a_i^{n_i} f(\Delta G_r) \,, \qquad (3)$$

where r_{net}, the overall rate of reaction, is the quantity directly measured , k_0 stands for a rate constant, S_e, the effective surface area, corresponds to the total area of the sites of different free energy (point defects, dislocations, pits, twin or grain boundaries, microfractures, edges, ledges…) exposed to the aqueous phase (Helgeson et al. 1984; Blum & Lasaga, 1987; Schott et al. 1989), E_a is the apparent activation energy, the $a_{H^+,OH^-}^{n_{H^+,OH^-}}$ and $g(I)$ terms describe the dependence of the rate on fluid pH (H^+, OH^- activity) and ionic strength, respectively, and $\prod a_i^{n_i}$ accounts for the catalysis or inhibition of the reaction by the activity of the i*th* aqueous species (see definition of symbols in Table 3). The last term, where ΔG_r stands for the Gibbs free energy change for the dissolution or growth reaction, describes the dependence of the overall rate on the departure from equilibrium. At a given temperature (150°C), pH (pH_T = 9) and ionic strength of the present study experiments Eq. (3) simplifies to:

$$r_{net} = k_+ A_e \prod a_i^{n_i} f(\Delta G_r) \,. \qquad (4)$$

where k_+ stands for albite dissolution rate constant at the temperature and pH of the experiment. $f(\Delta G)$ must satisfy two conditions: at equilibrium$f(\Delta G_r) = 0$, which guaranties the compatibility of kinetics with thermodynamics, and $f(\Delta G_r) = 1$ for far from equilibrium dissolution. The exact form of the function f depends on the kinetic mechanisms and represents a difficult question to answer. If a single step controls the reaction rate (Boudart, 1976) or if steady state conditions are met and the magnitude of ΔG_r for each elementary reaction is not much greater than RT (Nagy et al., 1991), the following simplified form can be derived from the Transition State Theory (TST, Aagard and Helgeson, 1982, Lasaga, 1998, Schott et al., 2009)

$$f(\Delta G) = [1 - exp(\Delta G_r / \sigma RT)], \qquad (5)$$

where σ stands for the Temkin's stoichiometric number, which is equal to the ratio of the rate of destruction of the activated complex relative to the overall reaction (it was assumed to equal 3 in the case of albite). Noting that the net rate of an elementary reversible reaction is the difference between

forward and backward reactions rates ($r_{net} = r_+ - r_-$), the combination of Eq. (3-4) with $r_+ = k_+ A_e \prod a_i^{n_i}$ yields the classical relation:

$$r_{net} = r_+[1 - exp(\Delta G_r/\sigma RT)]\,. \quad (6)$$

It should be noted that non-linear rate laws of the form $f(\Delta G_r) = [1 - exp(\Delta G_r/\sigma RT)]^n$ have been applied both for mineral dissolution and growth occurring at dislocation outcrops (Burch et al., 1993; Hellmann and Tisserand, 2006; Lasaga and Luttge, 2001; Shiraki and Brantley, 1995; Teng et al., 2000, 2004). Regarding the impact of the $\prod a_i^{n_i}$ term, it has been shown that the dissolution of several aluminosilicate minerals, including albite, was inhibited by aqueous aluminum (Oelkers et al., 1994; Gautier et al., 1994; Devidal et al., 1997; Carroll and Knauss 2005; Oelkers et al., 2008). In the present study the impact of Al on albite dissolution rate was described based on the results of Oelkers et al. (1994) on albite dissolution at pH 9 and 150°C (see Supplementary Information).

The accurate and unambiguous quantification of albite effective surface area S_e is very difficult, not only because the hydrolysis process occurs primarily at selective sites on the mineral surface, but because these sites autolocate and grow to form etch pits, which implies it is necessary to take into account the development of the process not only with time but also in space coordinates (Boldyrev, 1979). In the present study, albite dissolution rates were normalized to the BET surface area, which can be significantly greater than the effective surface area but can be accurately measured (including as a function of the reaction progress). Dissolution rates reported in this work should be thus considered as apparent rates.

2.9 Relaxation kinetics analysis of precipitation data

When a system at equilibrium is perturbed by a sudden temperature, pressure or pH change, its relaxation to a new chemical equilibrium can be described within the framework of relaxation kinetics originally developed by Eigen and de Maeyer (1963). When the displacement from equilibrium is slight, the progress of the system towards the new equilibrium can be described by a first order law:

$$C_t - (C_{eq})_2 = \left[(C_{eq})_1 - (C_{eq})_2\right].e^{-t/\tau} \quad (7)$$

the derivative of which with respect to time is given by

$$\frac{\partial C}{\partial t} = r_{net} = -\frac{\left[(C_{eq})_1 - (C_{eq})_2\right]}{\tau} e^{-t/\tau}, \quad (8)$$

where $(C_{eq})_1$ and $(C_{eq})_2$ are the equilibrium concentrations of one of the characteristic chemical species involved in the reaction before and after the temperature change. C_t is the species concentration at the time t and τ is a time parameter known as relaxation time. Eqs. (7-8) have been used in particular to quantify the growths of boehmite and gibbsite initiated by pH-jumps (Bénézeth et al., 2008) or of magnesite initiated by temperature-jumps (Saldi, 2009; Schott et al., 2012).

2.10 Interpretation of Si isotope data

Three main mechanisms, surface exchange, dissolution/precipitation and solid-state volume diffusion, could be invoked to explain the exchange of stable isotopes between a solid and the fluid at chemical equilibrium (Schott et al., 1989; Heberling et al., 2016; Harrison et al., 2022). Surface exchange and dissolution/precipitation are likely to participate in the observed exchanges in the outermost layers of the crystals accessible to the fluid, whereas solid-state diffusion could contribute to the exchanges occurring deeper in the crystals. Selecting the right rate controlling mechanism requires in particular to quantify the kinetics of isotope exchange and to express the isotope exchange controlled by dissolution/precipitation.

2.10.1 Kinetics of isotope exchange between the fluid and the solid

Following the approach taken by earlier workers (e.g., Criss et al., 1987; Johnson et al., 2002; Stamm et al., 2019), the extent of ^{28}Si/^{29}Si isotope exchange toward isotope equilibrium can be described by:

$$F = \frac{^{29/28}Si(t) - ^{29/28}Si(0)}{^{29/28}Si(eq) - ^{29/28}Si(0)}, \quad (9)$$

where $^{29/28}Si(t)$ is the fluid ^{29}Si to ^{28}Si ratio at time t, $^{29/28}Si(0)$ is the value of the same ratio at the beginning of the experiment (t = 0) and $^{29/28}Si(eq)$ its value at isotopic equilibrium. Note that $^{29/28}Si$ is equal to f_{29}/f_{28} (see f definition in Table 3). The $^{29/28}Si(eq)$ value was corrected for the change with time of the fluid volume and albite dissolution at the beginning of the run. Substituting F in the general rate equation produces:

$$\frac{-d(1-F)}{dt} = k_n(1-F)^n, \quad (10)$$

where k_n represents the rate constant with reaction order n. Isotope exchange reactions typically follow either a first-order (n = 1) or a second-order (n = 2) rate law (Criss et al., 1987; Johnson et al.,

2002; Welch et al., 2003; Li et al., 2011; Stamm et al., 2019). Integration of Eq. (10) for first-order and second-order rate laws yields the following linear forms:

$$\ln(1-F) = -k_1 t \text{ for } n = 1 \quad (11)$$

$$\frac{F}{(1-F)} = k_2 t \text{ for } n = 2 \quad (12)$$

Isotope exchange rate constants for the first-order and second-order rate laws can be quantified by fitting *F* experimental values to Eq. (11) and Eq. (12), respectively.

2.10.2 Isotope exchange controlled by albite dissolution/precipitation at equilibrium

Assuming that $^{29}Si/^{28}Si$ isotope exchange between the fluid and albite at equilibrium is controlled by albite forward and backward dissolution reactions ($r_{net} = r_+ - r_- = 0$) and neglecting the isotope fractionation due to both dissolution and precipitation, the temporal evolution of silica concentration and silicon isotope concentrations can be described with a set of mass balance equations (Zhu et al., 2016, 2020):

$$\begin{cases} [Si]^{t+1} = (v_{ab} r'_+ - v_{ab} r'_-)\Delta t + [Si]^t \\ \left[^{28}Si\right]^{t+1} = \left(v_{ab} f_{28,ab} r'_+ - v_{ab} f_{28,ab} r'_-\right)\Delta t + f_{28,t}\left[^{28}Si\right]^t \\ \left[^{29}Si\right]^{t+1} = \left(v_{ab} f_{29,ab} r'_+ - v_{ab} f_{29,ab} r'_-\right)\Delta t + f_{29,t}\left[^{29}Si\right]^t \end{cases} \quad (13)$$

where r'_+ and r'_- stand for albite dissolution and precipitation rate, respectively (see definition in Table 3). For a batch reactor, assuming constant dissolution and precipitation rate constants, Eq. (13) can be solved analytically:

$$\begin{cases} f_{28,t} = f_{28,ab} - \left(f_{28,ab} - f_{28,t0}\right)\left(\frac{v_{ab} r'_+ - v_{ab} r'_-}{[Si]^{t0}} t + 1\right)^{\frac{-v_{ab} r'_+}{v_{ab} r'_+ - v_{ab} r'_-}} \\ f_{29,t} = f_{29,ab} - \left(f_{29,ab} - f_{29,t0}\right)\left(\frac{v_{ab} r'_+ - v_{ab} r'_-}{[Si]^{t0}} t + 1\right)^{\frac{-v_{ab} r'_+}{v_{ab} r'_+ - v_{ab} r'_-}} \end{cases} \quad (14)$$

One obtains two equations for two unknowns (r'_+ and r'_-). Steady-state rates can be fitted to experimental data of $f_{28,t}$ and $f_{29,t}$. In practice, $f_{28,t}$ and $f_{29,t}$ are not sensitive to r'_- unless the percentage of Si precipitated is large relative to the solution [Si]. This means that the dissolution rate r_+ can be measured while Si precipitation occurs (Zhu et al., 2016).

With r'_+ fixed by the Si isotope ratios, r'_- can be derived from the mass balance for [Si] in Eq. (13). In practice, $f_{28,t}$ and $f_{29,t}$ are not independent in the experiments because $^{30}Si/^{28}Si$ are fixed. Similarly, the mass transfer rate of Al (from solutions to solids) can be calculated from a mass balance equation for Al similar to that for Si in Eq. (13).

357 The mass balance for Si alone cannot distinguish between the reverse reaction (albite
358 precipitation) and secondary phase precipitation. Considering in addition the mass balance for Al,
359 however, it is possible checking if the ratio of Al to Si removal from the solution is consistent with
360 albite precipitation.

361 # 3. RESULTS

362 ## 3.1 SEM examination of solids before and after reaction

363 SEM micrographs of albite grains were taken before reaction (Fig. 1) and after the experiments
364 (Fig. 3). The unreacted albite grains present a rather rough surface with various morphologic features
365 and occasionally small zones enriched in other feldspar-bearing elements, i.e., K, Ca and Ba (see
366 whitish areas in Fig. 1a), as revealed by EDX spot analyses. EDX analyses are consistent with XRD data
367 that show the presence of small amounts of anorthite and microcline. Albite post-reaction samples
368 exhibit widespread dissolution features, consisting of diffuse etch pits and grooves generated by
369 pervasive dissolution along line defects. Several feldspar grains also display slightly rounded shapes
370 due to dissolution at corners and edges. Because of the higher fluid volume to solid mass ratio, these
371 features are more pronounced in the solid recovered after the experiment Ab-02 (Fig. 3c-d) than in
372 the solid from Ab-01 (Fig. 3a-b). Intense dissolution marks are also apparent on the albite grains
373 reacted at 180 °C (Ab-03), which underwent precipitation at 150 °C during the second stage of the
374 experiment (Fig. 3e-f). These albite grains show the presence of small size precipitates (0.5 – 4 µm),
375 which were identified as mixtures of albite and K-feldspar (Fig. 4). Albite grains which underwent short
376 (8 hours, Ab-06) but very far-from-equilibrium interaction (ΔG_r = -64 kJ/mol) in mixed-flow reactors
377 also exhibit a significantly altered mineral surface (Fig. 3g-h), with similar dissolution features.

378 The albite sample recovered at the end of Ab-01 dissolution run showed an important increase
379 of the BET specific surface area of 110%. Albite grains reacted far from equilibrium (ΔG_r= - 30 kJ.mol^{-1})
380 in a mixed-flow reactor exhibited a similar 110 % increase in BET specific surface area (run Ab-05)
381 after only 26 hours of reaction, whereas a 78% increase was observed after only 8 hours of reaction
382 (ΔG_r= - 64 kJ.mol^{-1}, run Ab-06).

3.2 Reacting solutions elemental data and derived rates of albite dissolution and precipitation

The results of the albite batch experiments are listed in Table 4 (albite dissolution at 150°C, run Ab-01), Table 5 (albite dissolution at 150°C, run Ab-02) and Table 6 (albite dissolution at 180°C and precipitation at 150°C, run Ab-03) together with the Gibbs free energy of the reaction and albite overall dissolution/precipitation rates calculated from Si release/uptake to/from the solution. Albite dissolution rates determined via mixed-flow reactor experiments (150°C, pH=9) at far from equilibrium conditions ($-64 \leq \Delta G_r \leq -28$ kJ.mol^{-1}) are listed in Table 7.

The concentration changes of Si, Al and Na during the course of albite dissolution at 150 and 180°C in the batch reactors are plotted in Fig. 5. It can be seen that constant values of concentrations and of albite ion activity product (IAP) (see Tables 4-6) are achieved in less than 15 days and are maintained until the end of the runs (up to 41 days). Albite K_{sp} values at 150 and 180°C derived in the present study ($K_{sp}(150) = -16.1 \pm 0.2$, $K_{sp}(180) = -15.15 \pm 0.2$) are within the range of values reported by Lu et al. (2022). During the precipitation run at 150°C a continuous decrease of Si, Al and Na concentrations was observed with a stoichiometry of elements uptake roughly consistent with albite precipitation (see Table 6). After ~60 days of reaction, Si, Al and Na concentrations attained a steady-state which correspond, within the uncertainties, to the value of albite solubility product determined in the present study ($LogK_{sp}(150) = -16.3$).

Albite dissolution rate constant at 150°C and pH 9 determined in this study by mixed-flow reactors at the dissolution plateau ($\Delta G_r \leq -45$ kJ/mol) is $k_+ = 3.5 \pm 0.5 \times 10^{-8}$ mol.m^{-2}.s^{-1}, a value in agreement with those determined by Oelkers et al. (1994) and Hellmann and Tisserand (2006) with mixed-flow reactors at the same temperature and pH. Albite initial dissolution rates determined with batch reactors (see Table 4-5 and Fig 5) are significantly faster ($r_{net} = 1.2 \times 10^{-7}$ and 1.0×10^{-7} mol.m^{-2}.s^{-1} for run Ab-01 and Ab-02, respectively) likely because of the rapid dissolution of the small anorthite component of the solid (cf. Oelkers and Schott, 1995; Gudbrandson et al., 2014) and the presence of some ultrafine particles and strained crystal areas produced during samples preparation (grinding), which cannot be totally removed by ultrasonic cleaning (cf. Schott et al., 1981, 1989). For each run the rate derived from the first sampling, affected by such preferential dissolution, was thus discarded. Stoichiometric Al release with respect to Si was observed during dissolution, resulting in similar albite dissolution rates based either on Si or Al release. In Fig. 6 albite overall dissolution rate at 150 and 180°C have been plotted as a function of the Gibbs free energy of the dissolution reaction. With the

k_+ value determined in mixed-flow experiments at 150°C and extrapolated to 180°C using the Arrhenius equation and E_a = 56 kJ/mol ($k_{+(180°C)}$ = 10×10^{-8} mol.m^{-2}.s^{-1}), the rates reported in Fig. 6 appear to follow a simple TST rate law (Eqs. 5-6) if rate inhibition by aqueous Al is taken into account (see Appendix 1 in Supplementary Material).

The aqueous concentrations of Si and Al during albite precipitation at 150°C are plotted in Fig. 7 as a function of time. The solid lines in this figure represent a fit of Si and Al concentrations to Eq. (7), which shows that the relaxation kinetics approach accurately describes the approach to equilibrium with a value of the relaxation time τ equal to 25.4 days. The dependence upon saturation state of the precipitation rates derived from Eq. (7) for both Si and Al data, and their adherence to the TST rate law (Eq. 6) can be assessed with the aid of the Log-Log plot of net rates (r_{net}) against the degree of supersaturation expressed by the term ($\Omega^{1/3} - 1$). This plot (Fig. 8) shows that the precipitation rates are consistent with an order of reaction n = 1 (goodness of the fit, r^2 = 0.978) that is in accord with Eq. (5). The y-axis intercept of the regression line drawn through the data represents the dissolution rate constant k_+ associated to the precipitation reaction (Eq. 4). The derived value of k_+ is equal to 9.4×10^{-10} mol.m^{-2}.s^{-1} (Si data) and 8.7×10^{-10} mol.m^{-2}.s^{-1} (Al data). The overall rate of albite dissolution and precipitation at 150°C and pH 9 is plotted in Fig. 9 as a function of the Gibbs free energy of albite dissociation reaction. A good adherence of experimental data to Eq. (6) can be observed but the value of the dissolution rate constant k_+ corresponding to precipitation is about 20 times lower than that for dissolution.

3.3 Si isotope composition of reacting solutions

The isotope compositions of the experimental solutions are reported in Tables A1-A3. The temporal evolution of ^{28}Si and ^{29}Si fractional abundances in solution, f_{28} and f_{29}, is shown in Fig. 10. During the two dissolution runs at 150°C and the dissolution run at 180°C f_{28} increased and f_{29} decreased monotonically. More specifically, at the beginning of the dissolution and far from equilibrium with albite ($\Delta G_r < \sim -7$ kJ/mole), f_{28} and f_{29} increased and decreased sharply, respectively; as equilibrium was approached ($\Delta Gr > \sim -5$kJ/mole), the variations in f_{28} and f_{29} decreased considerably and f values changed only slightly with time once equilibrium with albite was reached (shaded areas in Fig.10). Interestingly, however, a significantly greater variation of f_{28} and f_{29} with time during equilibrium with albite at 150°C was observed for run Ab-02 compared to run Ab-01.

During the first 35 days of the precipitation run (between 15 and 50 days of reaction, see Fig. 10e-f), both f_{28} and f_{29} remained almost constant. This *f* plateau was followed for t > 50 days by a significant increase of f_{28} and a decrease of f_{29}, which correspond to a marked decrease of Si (and Al, Na) concentrations but that tends to fade away at the longest reaction times.

3.3.1 Kinetics of isotope exchange between the fluid and the solid

Dissolution runs. The values of *F*, the extent of isotope exchange toward isotope equilibrium, calculated using Eq. (9), are listed in Tables A1-A3 of Appendix A, whereas, assuming a first order rate law for isotope exchange (Eq. 11), ln(1 – *F*) has been plotted as a function of time in Fig.11. It can be seen on this plot that the isotope exchange between albite and the fluid indeed follows a first order rate law once chemical equilibrium between albite and the fluid has been reached. The very fast rates of isotope exchanges observed at the beginning of the runs (t ≤ 3 days) correspond to a control of isotope exchange by the forward albite reaction (dissolution) as demonstrated by the good agreement between albite net dissolution rate and the calculated rate of isotope exchange. For greater reaction times (t ≥ 6 days), once chemical equilibrium between albite and the fluid had been achieved, a constant rate of isotope exchange was observed (constant slope, k_{ex}, of the plots ln(1 – *F*) = f(t)). The values at 150°C of the rate constants of isotope exchange k_{ex}, normalized to aqueous Si amount and albite BET surface, are equal to 7.4×10^{-11} mol.m^{-2}.s^{-1} (run Ab-01) and 7.3×10^{-10} mol.m^{-2}.s^{-1} (run Ab-02). For run Ab-02, an increase of k_{ex} value from 7.3×10^{-10} to 1.2×10^{-9} mol.m^{-2}.s^{-1} could be observed after about 25 days of reaction which corresponded to a slight drop in Si (Al) concentrations (Fig. 11b). At 180°C, once chemical equilibrium is reached, the corresponding value of k_{ex} is equal to 1.3×10^{-9} mol.m^{-2}.s^{-1}.

Precipitation run. The plot of ln(1 – *F*) as a function of time is shown in Fig. 11d. ln(1 – *F*) remained equal to 0 (0.0025±0.002) during the first 15 days of precipitation but decreased linearly with time at increasing times to the end of the run (55-77 days of reaction). The corresponding calculated values of the rate of Si isotope exchange are k_{ex} = 1.0×10^{-12} mol.m^{-2}.s^{-1} for the first 15 days of the reaction and k_{ex} =1.3×10^{-9} mol.m^{-2}.s^{-1} for the last part of the experiment if we exclude the last data point. Note that the extremely low value calculated for k_{ex} during the first 15 days of reaction along the highest Ω values ($6 \leq \Omega \leq 10$) reflect a negligible albite forward rate (dissolution) compared to its backward rate (precipitation), as insignificant Si isotope fractionation occurred during Si removal from the solution (albite precipitation).

3.3.2 Albite forward dissolution rates r_+ derived from Si isotope data

3.3.2.1 *Analysis of dissolution runs*

The rates of albite forward dissolution as well as the rates of Si exchange between the aqueous fluid and the mineral cannot be derived from a simple mass balance of dissolved Si. To retrieve albite forward dissolution rate r_+ and backward precipitation rate r_- (assuming Si (and Al) uptake from the solution corresponds to albite precipitation), Eqs. (13-14) were solved simultaneously with the aid of the Excel solver to obtain the best least-square fit of experimental f_{28} and f_{29} values. For this purpose two different scenario were assumed for the dependence of r_+ on reaction time and reaction Gibbs free energy. In the first scenario, a single, constant value of r_+ (independent of time and of Gibbs free energy), was assumed in accord with the fit of albite experimental dissolution rates at 150 and 180°C to Eq. (6). In the second scenario the r_+ value was allowed to vary continuously with time. The r_+ values determined for these two scenarios are summarized in Table 8.

Single r_+ value. Assuming in accord with Eq. (6), a single, constant, r_+ value independent of time and chemical affinity, it was not possible to obtain a good fit of f_{28} and f_{29} data to Eqs. (13-14) for the runs performed both at 150 and 180°C. At 150°C (runs Ab-01 and Ab-02), the best fit (R^2 = 0.91, Fig. S1) was obtained for $r_+ = 5\times10^{-10}$ mol.m^{-2}.s^{-1}, a value two orders of magnitude lower than that derived from Si (Al) release rates and application of Eq. (6) ($r_+ = 3.5\times10^{-8}$ mol.m^{-2}.s^{-1}) . At 180°C the best fit (not shown) was obtained for $r_+ = 7.5\times10^{-10}$ mol.m^{-2}.s^{-1}, a value about two orders of magnitude lower than that derived from Si release ($r_+ = 10\times10^{-8}$ mol.m^{-2}.s^{-1}).

Variable r_+ value. This scenario, unlike the first scenario, leads to an excellent fit of Si isotope data (R^2 = 1), as a different r_+ value was determined for successive couples of f_{28} and f_{29} data in each experiment. The match between calculated and measured f_{28} and f_{29} values can be seen on Fig. S2. At 150°C, calculated r_+ continuously decreased with time, reaching after ~162hrs (run Ab-01) and 150 hrs (run Ab-02) of reaction, values of about 1.5×10^{-10} mol.m^{-2}.s^{-1} and 1.5×10^{-9} mol.m^{-2}.s^{-1}, respectively, and kept roughly constant ($r_+ = 6.5\pm1.5\times10^{-11}$ and $7.5\pm1.5\times10^{-10}$ mol.m^{-2}.s^{-1} for run Ab-01 and Ab-02, respectively) after ~290 hrs of reaction. These r_+ values are near 2-3 orders of magnitude slower than those derived from Si release rates and application of Eq. (6) as shown by the plots as a function of ΔG_r of the r_+ values derived from Si isotope and Si concentrations data (Fig. 12). Also, it can be seen on Fig.12 that the r_+ values derived from Si isotope data are close to the corresponding r_{net} values deduced from measured Si concentrations as a function of time. However, assuming that the overall Si release rate ($r_{net} = r_+ - r_-$) is equal to r_+, thus that no Si precipitation occurred ($r_- = 0$), leads to a slight

overestimation of aqueous Si concentrations at near to equilibrium or equilibrium conditions (see Fig. 13). The Si isotopes derived r_+ values calculated at 180°C vary from 4.1×10^{-8} mol.m^{-2}.s^{-1} after the first few hours of reaction to $7.6 \pm0.8\times10^{-10}$ at equilibrium, whereas the r_+ value derived from the fit of Si release rates to Eq. (6) is equal 10×10^{-8} mol.m^{-2}.s^{-1}.

3.3.2.2 *Analysis of the precipitation run*

As for the dissolution runs, if a constant r_+ value independent of time and reaction affinity is assumed, then it is not possible to obtain a good fit of f_{28} and f_{29} data for precipitation at 150 °C. In contrast, assuming a continuous variation of r_+ with time (and thus reaction affinity) allows matching in a satisfactory way the experimental data ($R^2 = 1$), as it can be seen in Fig S3. During the first 240 hrs of precipitation (and $5.7 \leq \Delta G_r \leq 8.2$ kJ/mol) the calculated r_+ value was relatively constant and low ($r_+ \sim 10^{-11}$ mol.m^{-2}.s^{-1}). As precipitation continued and ΔG_r decreased, r_+ progressively raised and reached a value of $\sim1.9\times10^{-9}$ mol.m^{-2}.s^{-1} after 1125 hrs (~ 47 days) of precipitation (ΔG_r = 1.12 kJ/mol). The corresponding r_+ constant value derived from aqueous Si (and Al) data and application of Eq. (6) is equal to 9.4×10^{-10} mol.m^{-2}.s^{-1}.

4 DISCUSSION

4.1 Mechanisms controlling Si isotopes evolution during albite dissolution/precipitation

4.1.1 Far from equilibrium conditions

Dissolution. The rapid increase of aqueous f_{28} (and decrease of f_{29}) values during the first 6/20 hours of albite dissolution at 150 and 180°C together with the agreement between measured r_{net} values and r_+ values derived from the fit of f_{28}/f_{29} data to Eqs. (13-14) prove that the far from equilibrium ($\Delta G_r \leq$ - 7kJ/mol) Si isotope exchanges between fluid and albite are controlled by albite dissolution reaction.

Precipitation. Both the rate of isotope exchange ($k_{ex} = 1.0\times10^{-12}$ mol.m^{-2}.s^{-1}) and albite forward dissolution rate ($r_+ \sim 10^{-11}$ mol.m^{-2}.s^{-1}, Table 8) derived from f_{28}/f_{29} data during the first 15 days of precipitation ($5.7 \leq \Delta G_r \leq 8.2$ kJ/mol) are very small and much slower than albite average backward precipitation rate ($r_- \sim 10^{-9}$ mol.m^{-2}.s^{-1}). As a result, since precipitation (Si removal from the solution) does not induce a measurable change in the Si isotopic composition of the solution, f_{28} values of the fluid remain constant. With increasing reaction time (and decreasing ΔG_r values) an increase of f_{28}

(with a decrease of f_{29}) is observed following the development of albite forward dissolution reaction from recently precipitated material (see the discussion below).

4.1.2 Equilibrium or near equilibrium conditions

It is generally acknowledged that three main mechanisms could explain solid-fluid isotope exchange at chemical equilibrium between the solid and the fluid: surface exchange (i.e. without element (Si) addition or loss to/from the solid), dissolution/precipitation driven by Ostwald ripening, and solid diffusion (Géhin et al., 2021; Heberling et al., 2017; Harrison et al., 2022, 2023; Zhang et al., 2022; Subhas et al., 2017; Bernard et al., 2017).

The results of the present study show a good agreement between the values of the rate constants of isotope exchange, k_{ex}, and the forward/backward (r_+/r_-) dissolution-precipitation rates deduced from the analysis of Si isotope data using Eqs. (11-12) and (13-14). This demonstrates that Si isotope exchanges between albite and the fluid are controlled by albite dissolution/precipitation. Note that in all the experiments the determined rates of isotopic exchange at chemical equilibrium are related to a slight increase of f_{28} values, consistent with the contribution of albite forward dissolution reaction. However, r_+ and r_- values at equilibrium deduced from the fit of f_{28} and f_{29} data to Eqs. (13-14) are much lower than corresponding r_+ and r_- values deduced from the fit of Si (Al) aqueous concentrations to Eqs. (4-6) and corrected for dissolution inhibition by aqueous Al (Eqs. A1-A2 in the supplementary information). For example, at 150°C, equilibrium r_+ values generated from isotope data and Eqs. (13-14) are ~250 times (run Ab-01) and ~ 20 times lower (run Ab-02) than r_+ values derived from Si concentration data using Eqs. (4-6). At 180°C the r_+ value deduced from isotope data is 80 times lower than the corresponding value derived from aqueous Si concentrations. The data reported on Fig. 12 show, as already observed at 150°C, a continuous, monotonic, decrease in albite forward dissolution rate r_+ with the increase of ΔG_r to 6.5×10^{-11} mol.m^{-2}.s^{-1} (run Ab 01) and 7.5×10^{-10} mol.m^{-2}.s^{-1} (run Ab 02) compared to r_+ values predicted by Eqs. (4-6) of 3.5×10^{-8} (assuming no Al inhibition) and ~ 1.6×10^{-8} mol.m^{-2}.s^{-1} (assuming Al inhibition). It is worth noting the different pathway of rate decrease followed by the two experiments Ab-01 and Ab-02, both conducted at the same temperature but with a different solid/water ratio (Fig. 12). Because Ab-01 was conducted with a solid/fluid ratio 3 times higher than Ab-02, the system reached the thermodynamic equilibrium earlier, with a faster drop of r_{net} and $r_{+(iso)}$ relative to the r_+ value deduced from Si concentration data, as observed above. Although the calculated mass of dissolved albite is approximately the same for the two experiments (0.04 g and 0.03 g for Ab-01 and Ab-02, respectively), the initial surface area exposed to the fluid in Ab-01 was

three times larger and less affected, during a shorter time, by the far-from equilibrium dissolution reaction compared to the solid in Ab-02. The latter suffered more pervading effects of the reaction, as shown by the widespread formation of etch pits and deep trenches on the mineral grains after the experiment (Fig. 3c-d). The different surface topography developed during the reaction could explain the different $r_{+(iso)}$ pathways observed during the two experiments: non-linear, slightly faster with very low equilibrium values for Ab-01; linear, spanning a larger ΔG_r range and exhibiting higher values at equilibrium for Ab-02.

4.2 Insights on albite dissolution/precipitation mechanisms from the Si isotope-doping method

The analyses of fluid Si/Al concentration and Si isotope data lead to contrasting dependences of albite dissolution/precipitation rates on time and reaction affinity.

Assuming a constant albite effective surface area during the reaction and taking account of the inhibitory effect of aqueous Al, it is possible to describe the evolution of Si and Al aqueous concentrations at 150 and 180 °C until attainment of chemical equilibrium using the classical Eq. (4) derived from the application of the principle of detailed balancing to a reversible elementary reaction with a constant k_+ value and $k_+/k_- = K_{eq}$. Considering albite precipitation at 150 °C from the supersaturated solution (Ω ~10) generated by the applied perturbation method (see § 2.9), the evolution towards equilibrium of Si/Al aqueous concentration according to Eq. (4) required a fitted k_+ value much lower than that derived from the dissolution runs (9.4×10^{-10} vs. 3.5×10^{-8} mol.m^{-2}.s^{-1}). This contrast in k_+ values implies a discontinuity between the net dissolution and the net precipitation rates at $\Delta G_r = 0$ and seems to invalidate the principle of detailed balancing (see Fig. 9).

Forward albite dissolution rates r_+ derived from f_{28} values and application of Eqs. (13-14) clearly show, unlike r_+ values derived from Si/Al data analyzed using Eqs. (4-6), a considerable decrease with time and the approach of albite-fluid chemical equilibrium. By providing direct access to the forward dissolution rate, the isotope doping method provides invaluable information on the mechanisms controlling mineral dissolution as a function of time and distance from equilibrium.

The decrease of albite forward dissolution rate with time and the approach of equilibrium, demonstrated by Si isotope spiking data, likely reflects a change in the concentration and/or nature and reactivity of the surface sites controlling dissolution/precipitation as the reaction proceeds and ΔG_r values approach 0.

It has been already advocated in the past that the dependence of dissolution rate on distance from equilibrium depends on the availability of reactive sites at the mineral surface, such as steps, point defects, twin or grain boundaries, microfractures, crystal edges and corners (Chernov, 1984; Liang et al., 1996; Zhang and Nancollas, 1998; Lasaga and Lüttge, 2001; Dove et al., 2005; Lüttge et al., 2019). The dissolution (growth) of those solid crystals that exhibit a high density of reactive sites because of their small size, high surface roughness, and, in general, a poor crystallinity, is controlled by the direct adsorption of reactants to the reactive sites resulting in constant forward dissolution rates and in a linear dependence of the net rate on the fluid saturation state that could be described by Eqs. (4-6). Such linear rate laws have been indeed observed for the dissolution/precipitation kinetics of boehmite and gibbsite (Bénézeth et al., 2008), hydromagnesite (Gautier, 2012), kaolinite (Devidal et al., 1997) and in some cases for quartz (Berger et al., 1994; Liu and Zhu, 2016) and feldspars (Oelkers et al., 1994; Gautier et al., 1994) dissolution. In contrast, the dissolution rates of well crystallized minerals displaying few reactive surface sites can exhibit non-linear dependence on the saturation state. This results from a lower density of reactive sites at their surface and its decrease with the reaction progress and/or a shift of the controlling reaction mechanism from defect-assisted or etch pit-driven dissolution, where the reaction takes place at steps emanating from the dislocation centres, to simple ion adsorption/detachment at less reactive pre-existing steps and corners (see Lasaga and Lüttge, 2001; Dove et al., 2005; Lüttge, 2006). Both processes would lead to an apparent decrease of the dissolution rate constant. In particular the control of dissolution by etch pits nucleation at dislocation outcrops can lead to complex and, possibly, irreproducible non-linear rate laws. According to the BCF theory (Burton et al., 1951), at far from equilibrium conditions (and thus large negative values of the Gibbs free energy of the dissolution reaction), hollow-cored dislocations spontaneously open into etch pits and control dissolution. However, as the reaction proceeds towards equilibrium, hollow cores stop opening into etch pits at a critical value of ΔG_r (and solution saturation state). This shift from an etch pit-controlled to an etch pit-free and much slower pace dissolution mechanism at pre-existing edges and corners has been invoked to explain the abrupt decrease of albite dissolution rate observed at a given value of ΔG_r and the resulting highly non-linear behavior of its dissolution (Burch et al., 1993; Hellmann and Tisserand, 2006; Arvidson and Luttge, 2010). Note that because of the large energy spectrum shown by the different defects present at the crystal surface, the dissolution of crystals with different reaction history may exhibit a large range of pathways intermediate between those generated by the etch pit and etch pit-free controls (Lüttge, 2006; Arvidson and Lüttge, 2010; Fisher et al., 2012; Schott et al., 2012).

626 However, the results of the present study, in agreement with previous findings of Gautier et al.
627 (2001) on quartz, shows a decrease of the concentration of albite reactive sites with time even at far
628 from equilibrium conditions ($\Delta G_r \leq$ - 30 kJ/mol). The intense etch pit development occurring at albite
629 surface during only 8 to 24 hrs of dissolution in a mixed-flow reactor at 150°C and pH = 9 (see Figs. 3
630 and S4) is accompanied by a ~100 % increase of albite BET specific surface area and an approximate
631 25 to 60% decrease in Si outlet concentration thus resulting in a BET surface area-normalized
632 dissolution rate divided by a factor of ~2.3 to 5. The observed decrease of albite dissolution rate is
633 likely caused by a decrease of albite effective surface area. As already pointed out by Gautier et al.
634 (2001), Gratz et al. (1991) and Gratz and Bird (1992), the generated etch pit and micro-cracks walls
635 responsible for the surface area increase (see Fig. 3g-h) can consist of relatively unreactive negative
636 crystal facets that induce moving steps bunch at their perimeter.

637 During albite dissolution in the batch reactor of the present study, intense etch pits and micro-
638 crack formation developed comparable to that observed in mixed-flow reactors far from equilibrium
639 (see Fig. 3a-h) with a 110% increase of the powder BET specific surface area (run Ab-01). It is thus likely
640 that the observed apparent decrease of albite forward dissolution rate (and rate constant) observed
641 in these runs also resulted, at least partly, from a decrease of albite effective surface area driven by
642 the nucleation of etch pits and micro-cracks at surface defects followed by the formation of unreactive
643 negative crystals. The monotonic decrease with time (and increasing ΔG_r) of albite forward dissolution
644 rate r_+ derived from f_{28} data (see Fig. 12) strongly suggests a continuous decrease of the contribution
645 of etch pits and other reactive sites to dissolution rather than an abrupt switch from an etch pit
646 controlling mechanism to an etch pit-free controlling mechanism for a critical value of ΔG_r. The switch
647 from an etch pits/surface defects dissolution control to an etch pits/surface defects-free control can
648 occur but the large free energy spectrum presented by the different surface defects may prevent to
649 observe an abrupt drop in r_+ and r_{net} for a given ΔG_r value. Another remarkable result of the present
650 study is that the plots as a function of the free energy of r_{net} and r_+ derived from Si isotope data are
651 almost indistinguishable (see Fig. 12). This further confirms that the observed decrease in dissolution
652 rates as equilibrium is approached is not due to the increase in the contribution of the backward
653 reaction and r_-, but mainly to the decrease of r_+ in conjunction with the decrease in the density of the
654 most reactive sites yielding with time an increasing control of dissolution by the less reactive steps
655 generated by etch pits opened during albite early dissolution.

At the onset of precipitation initiated by the temperature decrease to 150°C during run Ab-03 ($\Omega \sim 10$, $\Delta G_r = 8.1$ kJ.mol^{-1}), the value of the net precipitation rate, r_{net}, deduced from the evolution of Si/Al concentrations is equal to 1.2×10^{-9} mol.m^{-2}.s^{-1} with a r_+ value derived from Eq. (5), which assumes a linear growth mechanism, equal to 9.4×10^{-10} mol.m^{-2}.s^{-1}. However, the corresponding r_+ value deduced from Si isotope data ($r_+ \sim 10^{-11}$ mol.m^{-2}.s^{-1}) is near 2 orders of magnitude slower. This, together with the discontinuity observed in overall dissolution/precipitation rates near equilibrium ($-2 \leq \Delta G_r \leq +2$ kJ.mol^{-1}, see Fig. 9) suggests that precipitation was not controlled by the simple incorporation of growth units at kink sites because of the scarcity of these sites. This is confirmed by the SEM images of albite grains after reactions showing the presence on their surface of small size precipitates (0.5 – 4 μm) which were identified by EDX spectroscopy as mixtures of albite and K-feldspar (Fig. 4). Interestingly, as the system relaxed towards equilibrium (with $\Omega < 2$, $\Delta G_r < 2.4$ kJ.mol^{-1}) and enough solid (likely poorly crystallized) precipitated at albite surface, r_+ raised to $\sim 1\times10^{-9}$ mol.m^{-2}.s^{-1} thus reflecting a significant increase of the density of reactive sites for dissolution/growth and a probable change in the precipitation controlling mechanism.

4.3 Implication for describing the weathering rates of primary silicate minerals in natural environments

Over the last twenty years, an abundance of literature has been devoted to the discrepancy between silicate dissolution rates measured in the laboratory and the field and its possible origin (see White and Brantley, 2003; Maher et al., 2009, and references therein). The causes put forward to explain this discrepancy include, on the one hand, the difficult quantification in the field of weathering controlling parameters such as the water flow, the porous media water content, the effective surface area of each mineral in contact with the reacting fluid, and the precipitation of secondary phases and, on the other hand, the exact mechanisms controlling mineral dissolution over time (Maher et al., 2009; Fisher et al., 2012). With regard to the latter, the exact form of the law describing the influence of chemical affinity on the rate of dissolution has received a great deal of attention, since the alteration of many silicates, particularly feldspars, occurs close to equilibrium (Maher et al., 2006; Maher et al., 2009; Goddéris et al., 2010).

The present study, thanks to the decoupling of forward and backward reaction rates by isotope tracing, shows that another important cause of slow alteration rates in the field may be the time-

dependent decrease in the density of the most reactive sites on the mineral surface. This leads to a considerable reduction, over two orders of magnitude, in the forward dissolution rate of albite and suggests, contrary to general belief, that the main cause of the reduction in overall alteration rate with reaction progress may be the reduction in the density of active sites on the albite surface and not the increase in the rate of the backward precipitation reaction. Quantifying in the field the nature, density and temporal evolution of the sites controlling the dissolution of silicate minerals such as albite appears to be very challenging, which calls into question the feasibility of a deterministic description of the alteration of these minerals, as already suggested by Arvidson and Luttge (2010).

5. CONCLUDING REMARKS

Albite dissolution and precipitation rates were measured in ^{29}Si-rich solutions at 150 and 180°C (dissolution) and 150°C (precipitation) over a wide range of the Gibbs free energy of reaction ΔG_r, including equilibrium and near equilibrium conditions. The ^{29}Si doping method allowed quantification of the contributions of albite forward dissolution rates and backward precipitation rates to the overall rate, in particular at equilibrium, when the overall reaction rate is equal to zero.

The major outcome of the present study is that albite forward dissolution rates, r_+, normalized to the initial BET surface area were found to decrease continuously and monotonically with increasing time and ΔG_r, reaching at chemical equilibrium values about 1.3 to 2.4 orders of magnitude lower than corresponding initial (far from equilibrium) values depending on the initial solid/fluid ratio. The greater the solid/fluid ratio, the greater the decrease in the forward velocity at equilibrium. This considerable decrease in r_+ values was accompanied by a concomitant increase in albite powder BET surface area with the formation of widespread dissolution features consisting of diffuse etch pits and grooves generated by pervasive dissolution along line defects. In contrast, albite net dissolution rate normalized to the initial BET surface area appeared to follow a classical TST-derived rate law, as illustrated by the linear dependence of r_{net} on $(\Omega^{1/3} - 1)$. These two observations suggest that the main cause of the decrease of albite net dissolution rate as equilibrium is approached is not the increasing impact of the albite backward precipitation reaction but the decrease of its effective surface area that induced an important reduction in the values of both r_+ and r_-. The reduction in effective surface area, which occurred despite a concomitant increase in BET surface area, was likely the result of the formation of unreactive etch pits behaving as negative crystal facets in addition to the non-opening into reactive etch pits of dislocations outcropping at the crystal surface for critical values of ΔG_r.

The evolution with time and reaction affinity of the effective surface area of albite crystals, which a priori present a small density of high energy sites, defects, and grain boundaries (and thus exhibit a rather low surface roughness) should be influenced by their history. In the present study, it is likely that the sample preparation, i.e., grinding, which generates defects at the sample surface, affected the subsequent evolution with time and ΔG_r of the sample effective surface area. The result is that albite samples with different histories and, consequently, surface topography, site densities, and energy distribution of reactive sites, could dissolve at distinctly different rates as a function of time and departure from equilibrium as proposed by Lüttge (2006), Arvidson and Lüttge (2010), Fisher et al. (2012), Schott et al., (2012).

Dissolution experiments as a function of the departure from equilibrium in isotope-spiked solutions, allowing to decoupling of the forward and backward reactions rates, performed with different solid/fluid ratios and samples with different histories and well-characterized effective surface area and surface morphology should help to better determine the rate laws controlling the dissolution of silicate minerals.

Acknowledgements

This study received financial support from CNRS to JS and from NSF EAR-1926734 and EAR-2242907 to CZ. KYC acknowledges the support of his employer for his analytical costs of silica isotope analyses. We would like to thank Alain Castillo for the technical assistance during the experimental part of the work and for conducting BET surface area analyses of the albite powders. Carole Causserand provided technical assistance during ICP-OES and AAS aqueous samples analyses. We also thank Stéphane Le Blond Du Plouy for his help with SEM powder observation analyses. GDS is grateful to Simon Blotevogel and Maximiliano Fastelli for their help with XRD analyses and Rietveld refinement and to Pascale Bénézeth for the financial support to the analytical part of the study. We are thankful to the Associated Editor Carl I. Steefel and two anonymous reviewers for their insightful comments that improved the original manuscript.

Data Availability

Data are available through Mendeley Data at: doi: 10.17632/tc8vrwzhmn.1

References

Arnórsson, S. and Stefánsson, A. (1999) Assesment of feldspar solubility constants in water in the range 0° to 350°C at vapor saturation pressures. *Am. J. Sci.* **299**, 173-209.

Aagard, P. and Helgeson, H.C. (1982) Thermodynamic and kinetic constraints on reaction rates among minerals and aqueous solutions. *Am. J. Sci.* **282**, 237-285.

Arvidson, R.S., and Luttge, A. (2010) Mineral dissolution kinetics as a function of distance from equilibrium – New experimental results. *Chem. Geol.* **269**, 79-86.

Bandstra, J.Z. et al. (2008) Compilation of mineral dissolution rates *In* Kinetics of Water-Rock Interaction, S.L. Brantley et al. Eds, 737-823, Springer.

Beig, M.S. and Lüttge, A. (2006) Albite dissolution kinetics as a function of distance from equilibrium: Implications for natural feldspar weathering. *Geochim. Cosmochim. Acta* **70**, 1402-1420.

Bénézeth, P., Palmer, D.A., Wesolowski, D.J. (2008) Dissolution/precipitation kinetics of boehmite and gibbsite: application of a pH-relaxation technique to study near-equilibrium rates. *Geochim. Cosmochim. Acta* **72**, 2429-2453.

Bernard, S., Daval, D., Ackerer, P., Pont, S., Meibom, A., 2017. Burial-induced oxygen-isotope re-equilibration of fossil foraminifera explains ocean paleotemperature paradoxes. *Nat. Commun.* **8**, 1–10.

Blum, A. and Lasaga, A.C. (1987) Monte Carlo simulations of surface reaction rate laws. In *Aquatic Surface Chemical Processes at the Particle-Water Interface* (ed. W. Stumm), pp 255-292, J. Wiley & Sons.

Boldyrev, V.V. (1979) Control of the reactivity of solids. In *Annual Review of Material Science* (ed. R.A. Huggins) **9**, 455-469. Palo Alto, California, Annual Reviews, Inc.

Boudart, M. (1976) Consistency between kinetics and thermodynamics. *J. Phys. Chem.* **80**, 2869-2870.

Burch, T.E., Nagy, K.L. and Lasaga, A.C. (1993) Free energy dependence of albite dissolution kinetics at 80° C and pH 8.8. *Chem. Geol.* **105**, 137-162.

Burton, W.K., Cabrera, N., Frank, F.C. (1951) The growth of crystals and the equilibrium structure of their surfaces. *Phil. Trans. R. Soc. Lond.*, Ser. **A 243**, 299-358.

772 Carroll, S.A. and Knauss, K.G. (2005) Dependence of labradorite dissolution kinetcs on $CO_{2(aq)}$, $Al_{(aq)}$,
773 and temperature. *Chem. Geol.* **217**, 213-225.

774 Chernov, A. A. Modern Crystallography III (1984) Springer-Verlag Ed.. 517 p.

775 Criss, R.E., Gregory, R.T. and Taylor, H.P. (1987) Kinetic-theory of oxygen isotopic exchange between
776 minerals and water. *Geochim. Cosmochim. Acta* **51**, 1099-1108.

777 Devidal, J.-L., Schott, J., Dandurand, J.-L. (1997) An experimental study of kaolinite dissolution and
778 precipitation kinetics as a function of chemical affinity and solution compostion. *Geochim.*
779 *Cosmochim. Acta* **61**, 5165-5186.

780 Dove, P. M., Han, N. and De Yoreo, J. J. D. (2005) Mechanisms of classical crystal growth theory
781 explain quartz and silicate dissolution behavior. *Proc. Natl. Acad. Sci. USA*, **102**, 15357–15362.

782 Eigen, M. and de Maeyer, L. (1963) In 'Technique of Organic Chemistry', vol. VIIIb, A. Weissenberger
783 Ed., Wiley, New York, 895 pp.

784 Fisher, C., Arvidson, R.S., and Luttge, A. (2012) How predictable are dissolution rates of crystalline
785 materials? *Geochim. Cosmochim. Acta* **98**, 177-185.

786 Gautier, J.-M., Oelkers, E.H. and Schott, J. (1994) Experimental study of K-feldspar dissolution rates
787 as a function of chemical affinity at 150° C and pH 9. *Geochim. Cosmochim. Acta* **58**, 4549-
788 4560.

789 Gautier, J.-M., Oelkers, E.H. and Schott, J. (2001) Are quartz dissolution rates proportional to B.E.T.
790 surface areas? *Geochim. Cosmochim. Acta* **65**, 1059-1070.

791 Gehin, A., Gilbert, B., Chakraborty, S., Stack, A.G., Allard, L.F., Robinet, J.C. and Charlet, L. (2021)
792 Long-Term ^{13}C Uptake by ^{12}C-Enriched Calcite. *ACS Earth Space Chem.* **5**, 998-1005.

793 Georg, R.B., Reynolds, B.C., Frank, M. and Halliday, A.N. (2006) New sample preparation techniques
794 for the precise determination of the Si isotope composition of natural samples using MC-ICP-
795 MS. *Chem. Geol.* **235**, 95-104.

796 Goddéris Y., François L.M., Probst A., Schott J. et al. (2006) Modelling weathering processes at the
797 catchment scale: the WITCH numerical model. *Geochim. Cosmochim. Acta* **70**, 1128-1147.

798 Goddéris, Y., Williams, J.Z., Schott J., Pollard, D., Brantley S.L. (2010) Time evolution of the
799 mineralogical composition of Mississippi Valley loess over the last 10 kyr: Climate and
800 geochemical modeling. *Geochim. Cosmochim. Acta* **74**, 6357-6374.

801 Gratz, A.J., Manne, S., and Hansma, P.K. (1991) Atomic force microscopy of atomic-scale ledges and
802 etch pits formed during dissolution of quartz. *Science* **251**, 1343-1346.

803 Gratz, A.J. and Bird, P. (1993) Quartz dissolution: Negative crystal experiments and a rate law.
804 *Geochim. Cosmochim. Acta* **57**, 965-976.

805 Gruber, C., Zhu, C., Georg, R.B., Zakon, Y. and Ganor, J. (2014) Resolving the gap between laboratory
806 and field rates of feldspar weathering. *Geochim. Cosmochim. Acta* **147**, 90-106.

807 Gudbrandsson, S., Wolff-Boenisch, D., Gislason, S.R., Oelkers, E.H. (2014) Experimental
808 determination of plagioclase dissolution rates as a function of its composition and pH at 22°C.
809 *Geochim. Cosmochim. Acta* **139**, 154-172.

810 Harrison, A.L., Schott, J., Oelkers, E.H., Maher, K., Mavromatis, V. (2022) Rates of carbon and oxygen
811 exchange between calcite and fluid at chemical equilibrium. *Geochim. Cosmochim. Acta* **335**,
812 369-382.

813 Harrison, A.L., Heuser, A., Liebetrau, V., Eisenhauer, A., Schott, J., Mavromatis V. (2023) Equilibrium
814 Ca isotope fractionation and the rates of isotope exchange in the calcite-fluid and aragonite-fluid
815 systems at 25 °C. *Earth Planet. Sci. Lett.* **603**, 117985.

816 Heberling, F., Paulig, L., Nie, Z., Schild, D. and Finck, N. (2016) Morphology controls on calcite
817 recrystallization. *Environ. Sci. Technol.* **50**, 11735-41.

818 Helgeson, H.C., Delany, J.M., Nesbitt, H.W., Bird, D.K. (1978) Summary and critique of the
819 thermodynamic properties of rock-forming minerals. *Am. J. Sci.* **278-A**, 1-229.

820 Helgeson, H.C., Murphy, W.M. and Aagard, P. (1984) Thermodynamic and kinetic constraints on
821 reaction rates among minerals and aqueous solutions. Rate constants, effective surface area,
822 and the hydrolysis of feldspars. *Geochim. Cosmochim. Acta* **48**, 2405-2432.

823 Hellmann, R. and Tisserand, D. (2006) Dissolution kinetics as a function of the Gibbs free energy of
824 reaction: An experimental study based on albite feldspar. *Geochim. Cosmochim. Acta* **70**, 364-
825 383.

826 Heřmanská, M., Voigt, M.J., Marieni, C., Declercq, J., Oelkers, E.H. (2022) A comprehensive and
827 internally consistent mineral dissolution rate database: Part I/ Primary silicate minerals and
828 glasses. *Chem. Geol.* **597**, 120807

829 Higgins, S. R., Jordan, G., and Eggleston, C. M. (2002) Dissolution kinetics of magnesite in acidic
830 aqueous solution: a hydrothermal atomic force microscopy study assessing step kinetics and
831 dissolution flux. *Geochim. Cosmochim. Acta* **66**, 3201–3210.

832 Holdren, G.R. Jr., and Berner, R.A. (1979) Mechanism of feldspar weathering – I. Experimental
833 studies. *Geochim. Cosmochim. Acta* **43**, 1161-1171.

834 Holland, T.J.B., Powell, R. (2011) An improved and extended internally consistent data set for phases
835 of petrological interest, involving a new equation of state for solids. *J Metamorph. Geol*. **29**, 333-
836 383.

837 Johnson, C.M., Skulan, J.L., Beard, B.L., Sun, H., Nealson, K.H. and Braterman, P.S. (2002) Isotopic
838 fractionation between Fe(III) and Fe(II) in aqueous solutions. *Earth Planet. Sci. Lett.* **195**, 141-
839 153.

840 Lasaga, A.C. (1998) *Kinetic Theory in the Earth Science*. Princeton University Press, New Jersey. 811
841 p..

842 Lasaga, A.C. and Luttge, A. (2001) Variation of crystal dissolution rate based on a dissolution
843 stepwave model. *Science* **291**, 2400-2404.

844 Lasaga, A.C., Soler J.M., Ganor, J., Burch, T.E., Nagy, K.L. (1994) Chemical weathering rate laws and
845 global geochemical cycles. *Geochim. Cosmochim. Acta* **58**, 2361-2386.

846 Lebedeva M.L., Fletcher, R.C., Brantley, S.C. (2010) A mathematical model for steady-state regolith
847 production at constant erosion rate. *Earth Surf. Proc. Land.* **35**, 508-524.

848 Liang, Y., Baer, D. R., McCoy, J. M. and LaFemina, J. P. (1996) Interplay between step velocity and
849 morphology during the dissolution of $CaCO_3$ surface. *J. Vac. Sci. Technol. A* **14**, 1368–1375.

850 Li, W.Q., Beard, B.L. and Johnson, C.M. (2011) Exchange and fractionation of Mg isotopes between
851 epsomite and saturated $MgSO_4$ solution. *Geochim. Cosmochim. Acta* **75**, 1814-1828.

852 Liu, Z., Rimstidt, J.D., Zhang, Y. and Zhu, C. (2016) A stable isotope doping method to test the range
853 of applicability of detailed balance. *Geochem. Perspect. Lett.* **2**, 78-86.

Lu, P., Zhang, G., Apps, J., Zhu, C. (2022) Comparison of thermodynamic data files for PHREEQC. *Earth-Science Rev.* **225**, 103888.

Luce, R.W., Bartlett, R.W., and Parks, G.A. (1972) Dissolution kinetics of magnesium silicates. *Geochim. Cosmochim. Acta* **36**, 35-50.

Lüttge, A. (2006) Crystal dissolution kinetics and Gibbs free energy. *J. Electron. Spectrosc.* **150**, 248–259.

Lüttge, A., Arvidson, R. S., Fischer, C. and Kurganskaya, I (2019). Kinetic concepts for quantitative prediction of fluid-solid interactions. *Chem. Geol*. **504**, 216–235.

Maher, K., Steefel, C.I., DePaolo, D.J., Viani, B.E. (2006) The mineral dissolution rate conundrum; Insights from reactive transport modeling of U isotopes and pore fluid chemistry in marine sediments. *Geochim. Cosmochim. Acta* **70**, 37-363.

Maher, K., Steefel, C.I., White, A.F. and Stonestrom, D.A. (2009) The role of reaction affinity and secondary minerals in regulating chemical weathering rates at Santa Cruz Soil Chronosequence, California. *Geochim. Cosmochim. Acta* **73**, 2804-2831.

Nagy, K.L., Blum, A.E., Lasaga, A.C. (1991) Dissolution and precipitation kinetics of kaolinite at 80°C and pH 3: the dependence on solution saturation state. *Am. J. Sci.* **291**, 649-686.

Navarre-Sitchler, A and Brantley, S.L. (2007) Basalt weathering across scales. *Earth Planet. Sci. Lett.* **261**, 321-334.

Oelkers E. H. and Schott J. (1995) Experimental study of anorthite dissolution and the relative mechanism of feldspar hydrolysis. *Geochim. Cosmochim. Acta* **59**, 2804-2831.

Oelkers, E.H., Schott, J. and Devidal, J.L. (1994) The effect of aluminum, pH, and chemical affinity on the rates of aluminosilicate dissolution reactions. *Geochim. Cosmochim. Acta* **58**, 2011-2024.

Oelkers, E.H., Schott, J., Gautier, J.-M., Herrero-Roncal, T. (2008) An experimental study of the dissolution mechanisms and rates of muscovite. *Geochim. Cosmochim. Acta* **72**, 4948-4961.

Palandri, J. and Kharaka, Y. (2004) A Compilation of Rate Parameters of Water-Mineral Interaction Kinetics for Application to Geochemical Modeling. U.S. Geological Survey, Open File Report 2004-1068.

881 Parkhurst, D.L. and Appelo, C.A.J.(2013) Description of input and examples for PHREEQC version 3—
882 A computer program for speciation, batch-reaction, one-dimensional transport, and inverse
883 geochemical calculations: U.S. Geological Survey Techniques and Methods, book 6, chap.
884 A43, 497 p., available only at http://pubs.usgs.gov/tm/06/a43/.

885 Pollet-Villard, M., Daval, D., Ackerer, P., Saldi, G.D., et al. (2016a) Does crystallographic anisotropy
886 prevent the conventional treatment of aqueous mineral reactivity? A case study based on K-
887 feldspar dissolution kinetics. *Geochim. Cosmochim. Acta* **190**, 294-308.

888 Pollet-Villard, M., Daval. D., Fritz, B., Knauss, K. G., et al. (2016b) Influence of etch pit development
889 on the surface area and dissolution kinetics of the orthoclase (001) surface. *Chem. Geol.* **447**,
890 79-92.

891 Saldi, G.D. (2009) Les cinétiques de dissolution et précipitation de la magnesite aux conditions
892 hydrothermales. PhD Thesis. Toulouse University, 184 p.

893 Schott, J., Berner, R.A., and Sjöberg, E.L. (1981) Mechanism of pyroxene and amphibole weathering –
894 I. Experimental studies of iron-free minerals. *Geochim. Cosmochim. Acta* **45**, 2123-2135.

895 Schott, J., Pokrovsky, O. S., and Oelkers, E.H. (2009) The link between mineral
896 dissolution/precipitation kinetics and solution chemistry. *Rev. Min. Geochem.* **70**, 207-258.

897 Schott, J., Brantley, S., Crerar, D., Guy, C., Borcsik, M. and Willaime, C. (1989) Dissolution kinetics of
898 strained calcite. *Geochim. Cosmochim. Acta* **53**, 373-382.

899 Schott, J., Oelkers, E.H., Bénézeth, P., Goddéris, Y., François, L. (2012) Can accurate kinetic laws be
900 created to describe chemical weathering? *C. R. Geoscience* **344**, 568-585.

901 Shiraki, R., and Brantley, S. L. (1995) Kinetics of near-equilibrium calcite precipitation at 100°C: An
902 evaluation of elementary reaction-based and affinity-based rate laws. *Geochim. Cosmochim.*
903 *Acta* **59**, 1457–1471.

904 Stamm, F.M., Zambardi, T., Chmeleff, J., Schott, J., von Blanckenburg, F. and Oelkers, E.H. (2019) The
905 experimental determination of equilibrium Si isotope fractionation factors among $H_4SiO^\circ_4$,
906 $H_3SiO_4^-$ and amorphous silica ($SiO_2 \cdot 0.32\ H_2O$) at 25 and 75 °C using the three-isotope method.
907 *Geochim. Cosmochim. Acta* **255**, 49-68.

908 Stefánsson, A., Gislason, S.R., Arnórsson, S. (2001) Dissolution of primary minerals in natural waters
909 II. Mineral saturation state. *Chem. Geol.* **172**, 251-276.

910 Subhas, A. V., Adkins, J.F., Rollins, N.E., Naviaux, J., Erez, J., Berelson, W.M., 2017. Catalysis and
911 chemical mechanisms of calcite dissolution in seawater. *Proc. Natl. Acad. Sci.* **114**, 8175–8180.

912 Teng, H. H. (2004) Controls by saturation state on etch pit formation during calcite dissolution.
913 *Geochim Cosmochim Acta* **68**, 253–262.

914 Teng, H., Dove, P., and De Yoreo, J. D. (2000) Kinetics of calcite growth: Surface processes and
915 relationships to macroscopic rate laws. *Geochim. Cosmochim. Acta* **64**, 2255–2266.

916 Voigt, M., Marieni, C., Clark, D.E., Gislason, S.R., Oelkers, E.H. (2018) Evaluation and refinement of
917 thermodynamic data bases for mineral carbonation. *Energy Procedia.* **146**, 81-91.

918 Welch, S.A., Beard, B.L., Johnson, C.M. and Braterman, P.S. (2003) Kinetic and equilibrium Fe isotope
919 fractionation between aqueous Fe(II) and Fe(III). *Geochim. Cosmochim. Acta* **67**, 4231-4250.

920 Zhang, Q., Peng, X., Nie, Y., Zheng, Q., Shangguan, J., Zhu, C. Bustillo, K.C., Ercius, P., Wang, L.,
921 Limmer, D.T., and Zheng, H. (2022). Defect-mediated ripening of core-shell nanostructure. *Nat.*
922 *Commun.* **13**, 1-10.

923 Zhang, J. and Nancollas, G. H. (1998) Kink Density and Rate of step movement during growth and
924 dissolution of an AB crystal in a nonstoichiometric solution. *J. Colloid Interface Sci.* **200**, 131–145.

925 Zhu, C., Liu, Z., Zhang, Y., Wang, C., Schearer, A., Zhang, G., Georg, R.B., Yuan, H.-l. and Rimstidt, J.D.
926 (2016) Measuring silicate dissolution rates using Si isotope doping. *Chem. Geol.* **445**, 146-163.

927 Zhu, C., Rimstidt, J.D., Zhang, Y.L., Kang, J.T., Schott, J., and Yan, Y.L. (2020) Decoupling feldspar
928 dissolution and precipitation rates at near-equilibrium with Si isotopes tracers: Implications for
929 modeling silicate weathering. *Geochim. Cosmochim. Acta* **271**, 132-153.

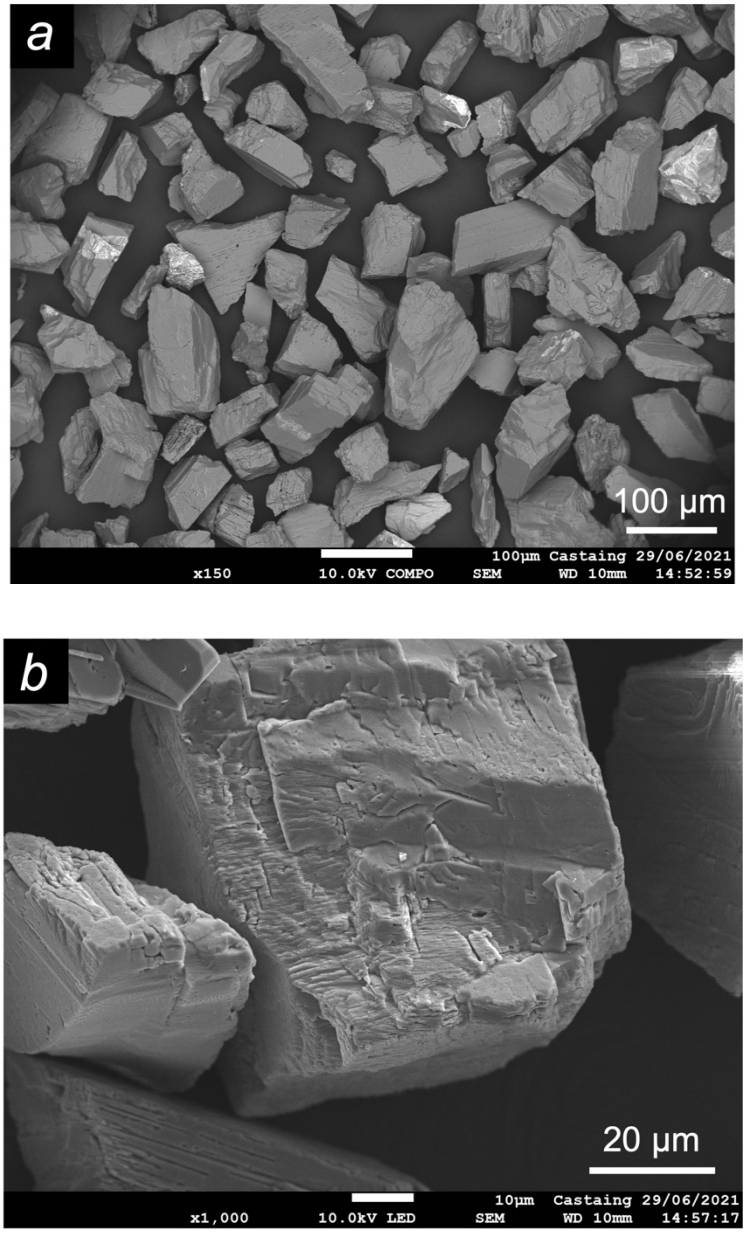

Fig.1. SEM images of the natural albite powder (53-106 µm) used for the experimental work. a) Back-scattered image of unreacted powder showing restricted grain bright areas enriched in K (5-10 wt %), Ba (10-28 wt%) or Ca (1-25 %). b) Details of single albite grains presenting only few fine particles at their surface.

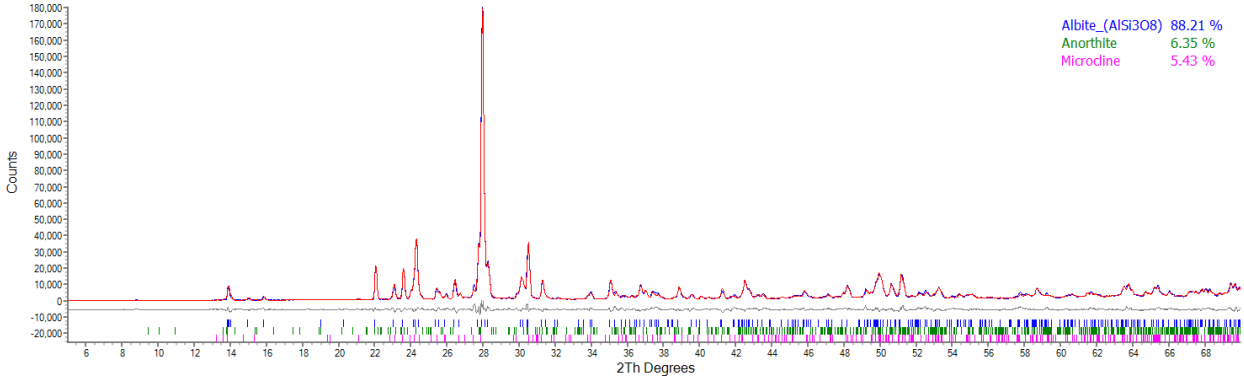

Fig. 2. XRD diffraction pattern of the albite sample used for the experimental study with the results of the Rietveld refinement showing that albite is the main mineral phase (88.2 %), with minor amounts of Ca in its composition (corresponding to 6.4 % wt of anorthite) and the presence of a small percentage of microcline (5.4 % wt). The uncertainties of the phase quantification are ≤ 0.08%.

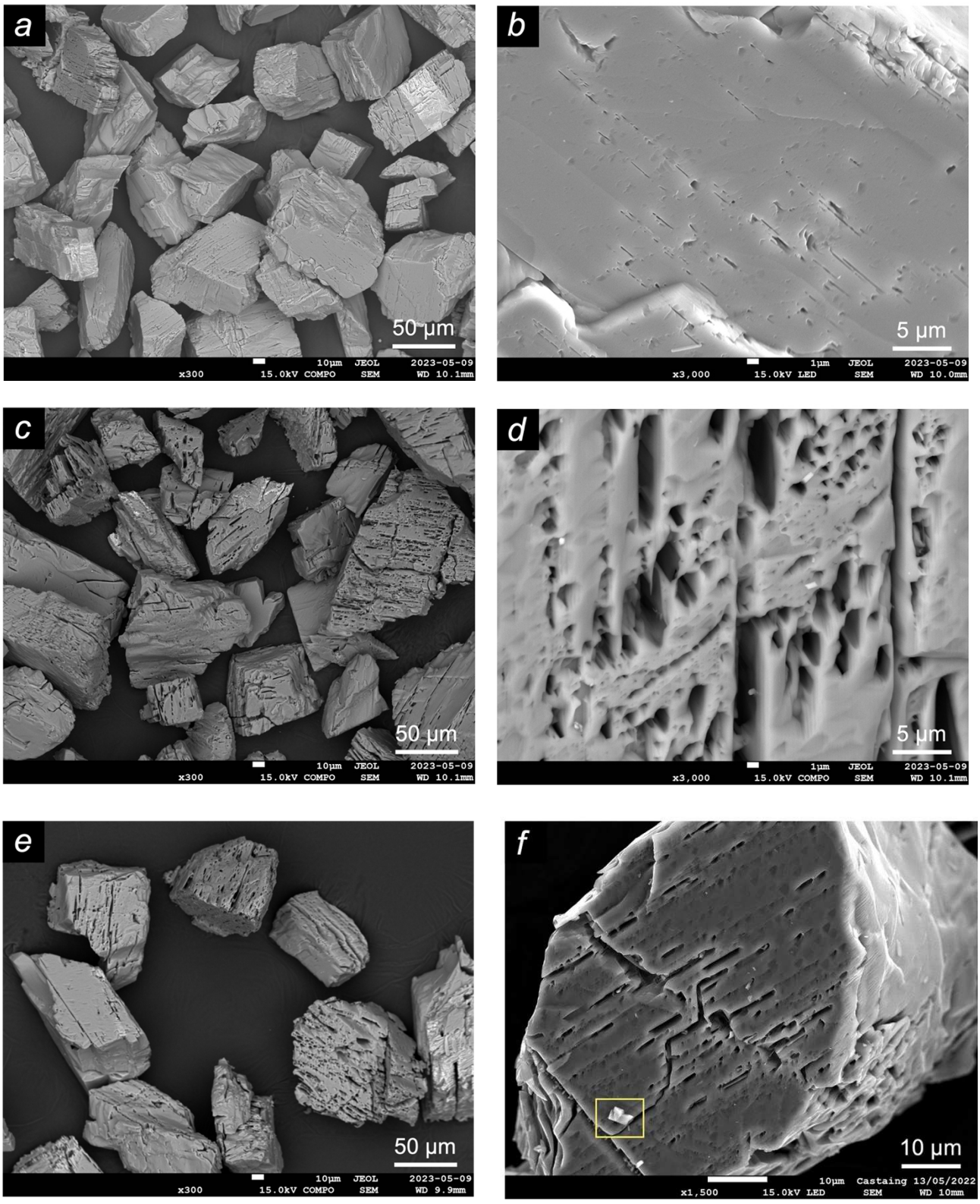
a
50 µm
10µm JEOL 2023-05-09
x300 15.0kV COMPO SEM WD 10.1mm
b
5 µm
1µm JEOL 2023-05-09
x3,000 15.0kV LED SEM WD 10.0mm
c
50 µm
10µm JEOL 2023-05-09
x300 15.0kV COMPO SEM WD 10.1mm
d
5 µm
1µm JEOL 2023-05-09
x3,000 15.0kV COMPO SEM WD 10.1mm
e
50 µm
10µm JEOL 2023-05-09
x300 15.0kV COMPO SEM WD 9.9mm
f
10 µm
10µm Castaing 13/05/2022
x1,500 15.0kV LED SEM WD 10mm

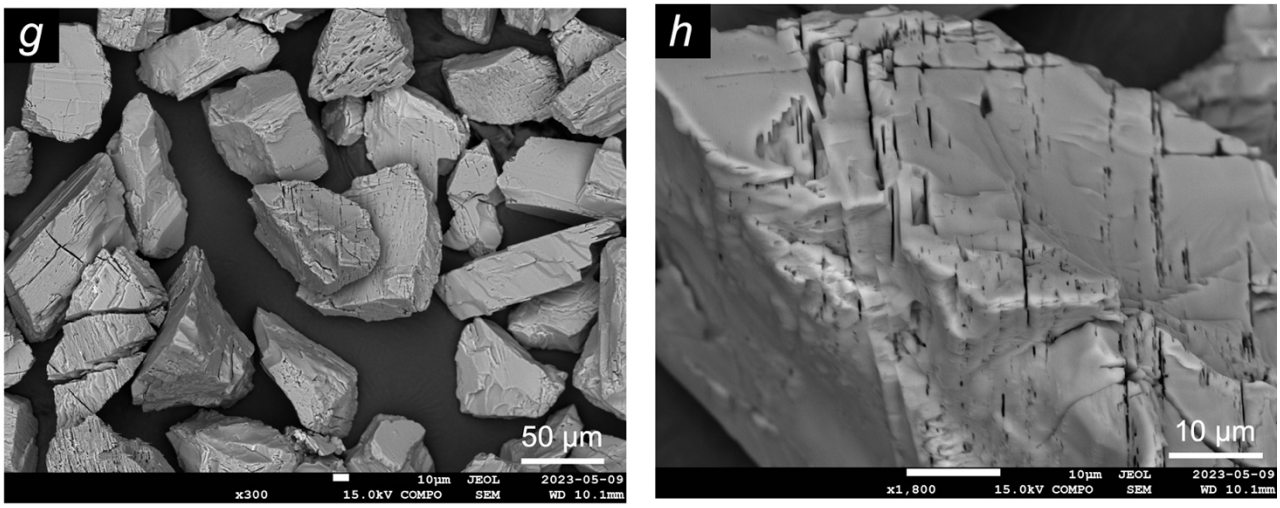

Fig. 3. SEM microphotographs of albite grains after reaction at pH = 9 and 150 and 180 °C. (a-b) Low magnification and detail of albite grains after the experiment Ab-01 (28 days, 150 °C). (c) General appearance of albite grains after experiment Ab-02 (41 days, 150 °C). (d) Detail of a grain surface from experiment Ab-02. (e-f) Albite grains reacted at 180 °C for 15 days and 61 days at 150 °C (expt. Ab-03). (g-h) Albite grains recovered after an 8 hour-long mixed-flow reactor experiment conducted at 150 °C (Ab-06).

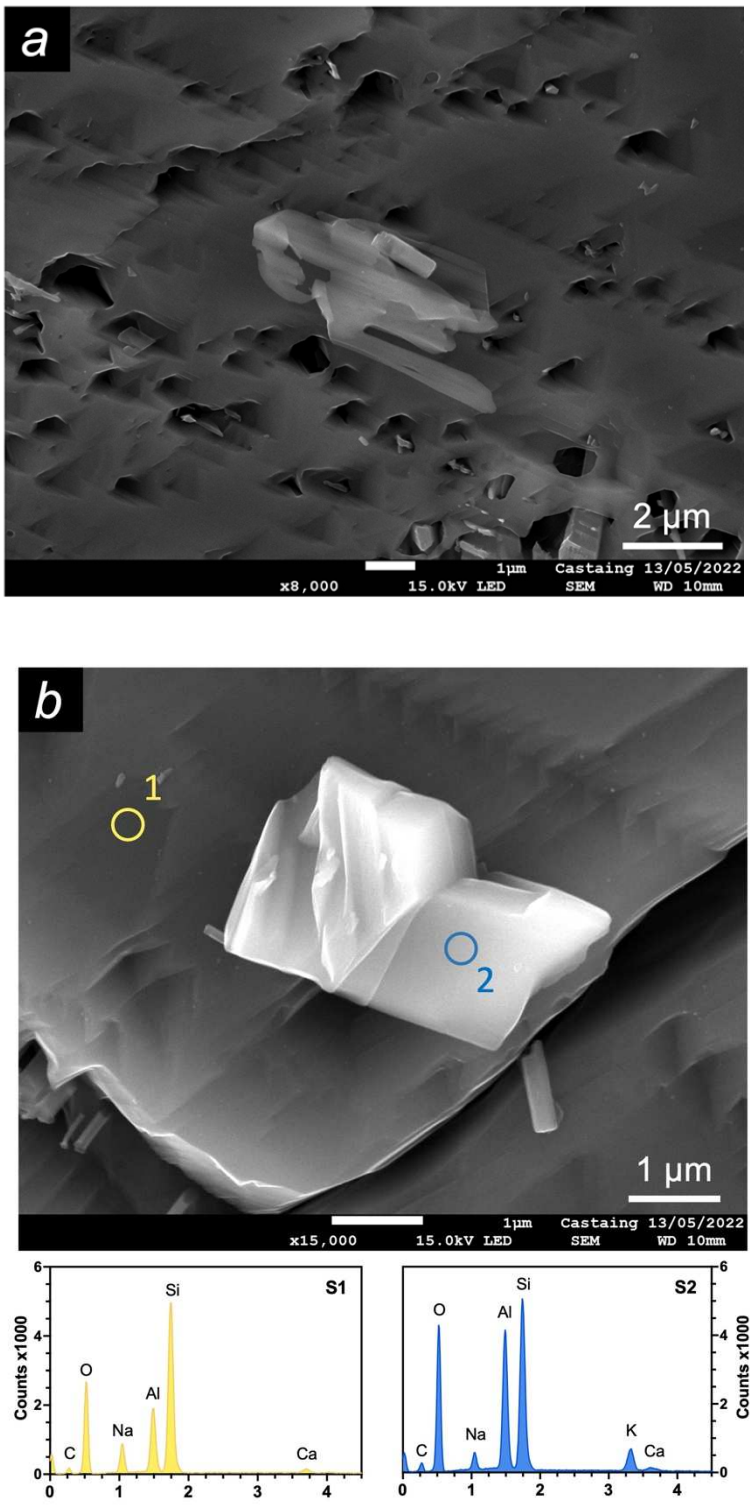

Fig. 4. SEM microphotographs of secondary precipitates formed on extensively leached albite grains during the second part of experiment Ab-03 at 150 °C. Geometric relationships and EDX analyses (b) suggest that the observed crystals are secondary alkali feldspars. Figure (b) is the magnified area of the small inset reported Fig. 3f.

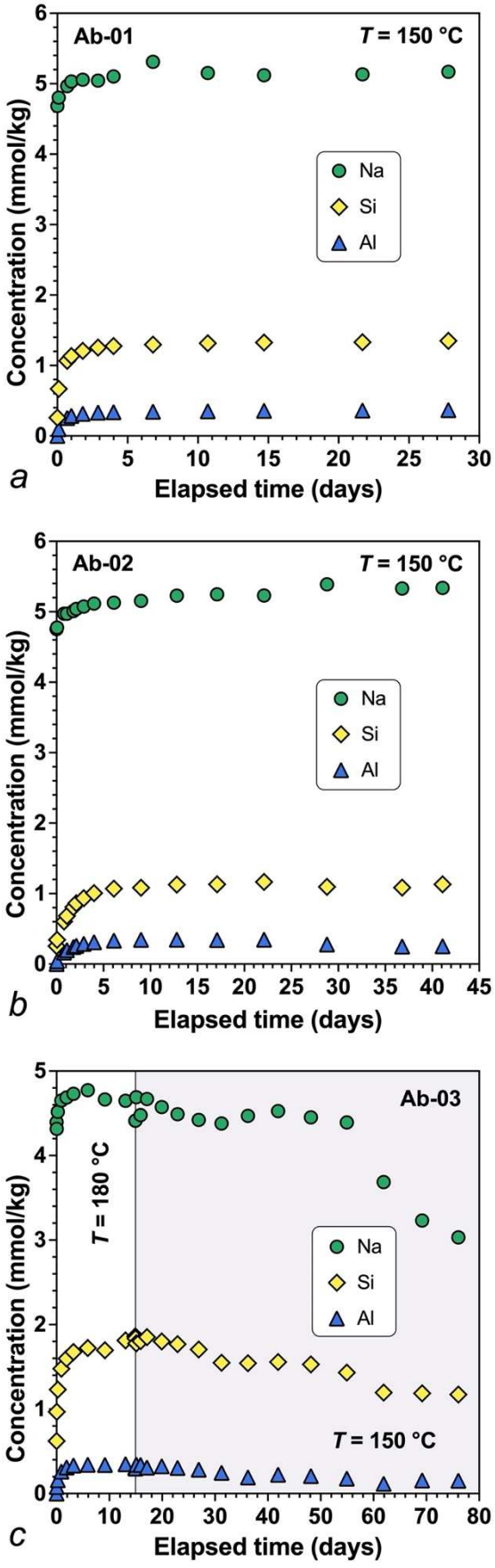

Fig. 5. Evolution of Na, Si, and Al concentrations during albite dissolution at 150°C and 180°C and precipitation at 150°C. (a) Albite dissolution at 150°C (run Ab-01); (b) albite dissolution at 150°C (run Ab-02); (c) albite dissolution at 180°C and precipitation (shaded area) at 150°C (run Ab-03).

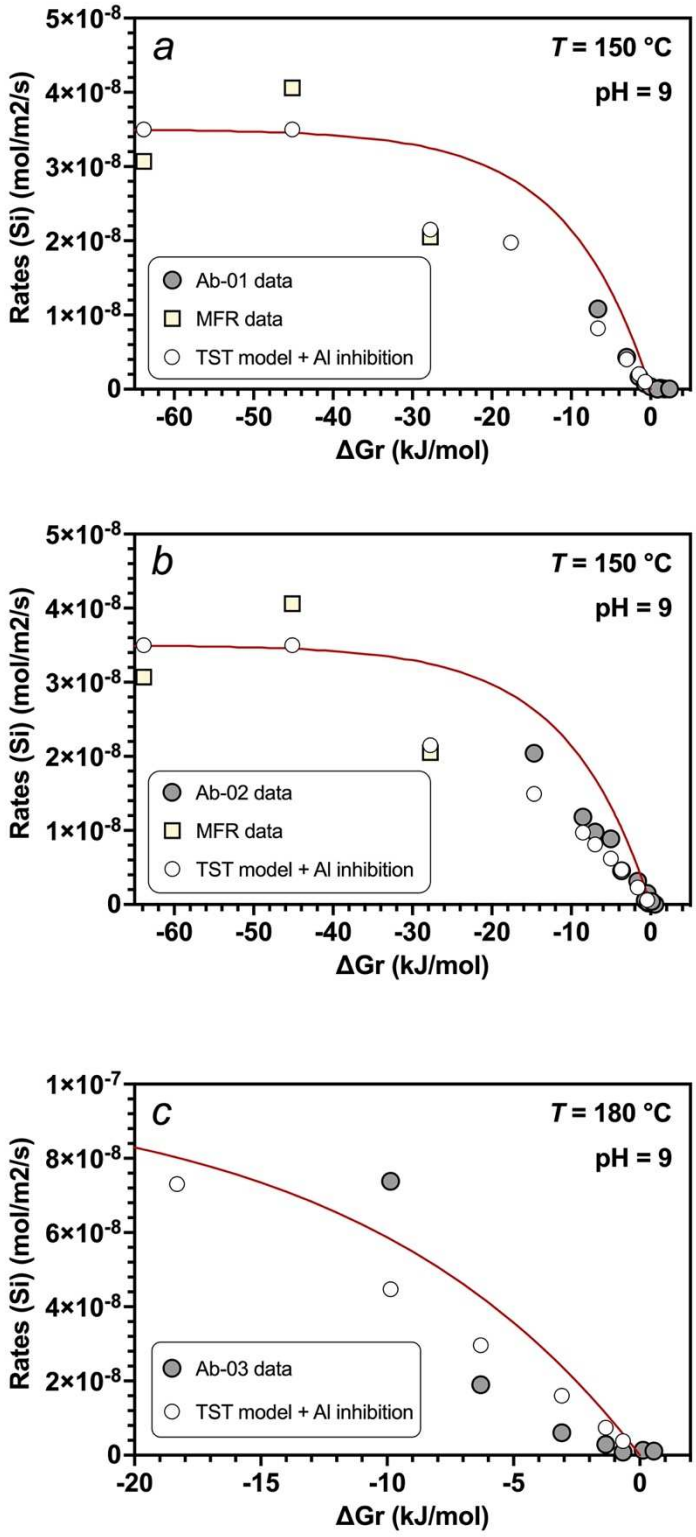

Fig. 6. Plots of Albite dissolution rates at pH 9 against the Gibbs free energy of reaction. (a) Run Ab-01 at 150°C; (b) run Ab-02 at 150°C; (c) run Ab-03 at 180°C. The grey circles and yellow squares are the experimental rates determined in batch and mixed-flow reactors, respectively; the white circles represent the TST-derived rates taking account of Al inhibition at 150 and 180°C (see text for details); and the red solid lines represent TST-derived rates assuming no Al inhibition. The dissolution rate constants used in the calculation of TST rates are $k_+ = 3.5\times10^{-8}$ and 10×10^{-8} mol/m^2/s at 150 and 180°C, respectively. For a closer view of the lowest rate data in proximity of the thermodynamic equilibrium with albite, the reader can refer to the plots of Fig. 12.

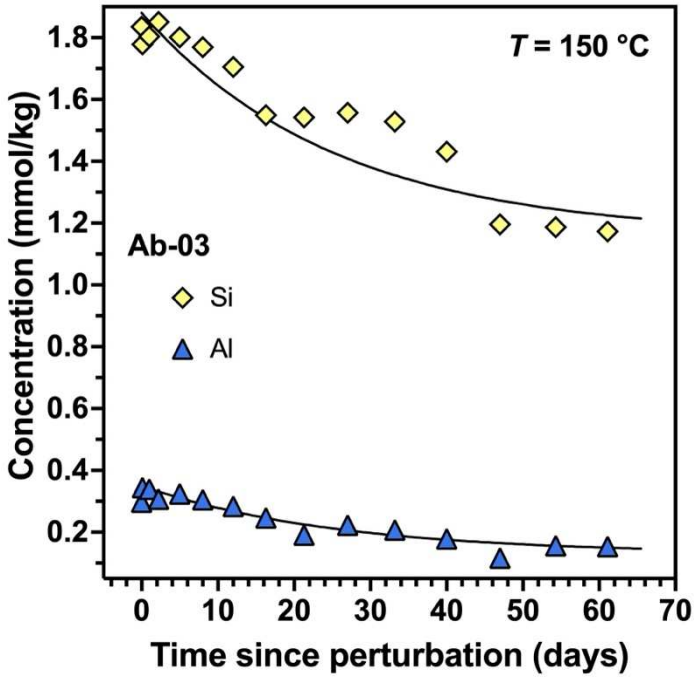

Fig. 7. Variation of Si and Al concentrations during the albite precipitation experiment at 150°C induced by temperature jump from 180°C (Ab-03). The symbols (circles for Si and triangles for Al) represent the experimental data whereas the lines stand for the fits of these data according to Eq. (7) with τ = 25.4 days. Note that the time 0 corresponds to 14.9 days on the plot of Fig. 5c, when temperature changed from 180 to 150 °C.

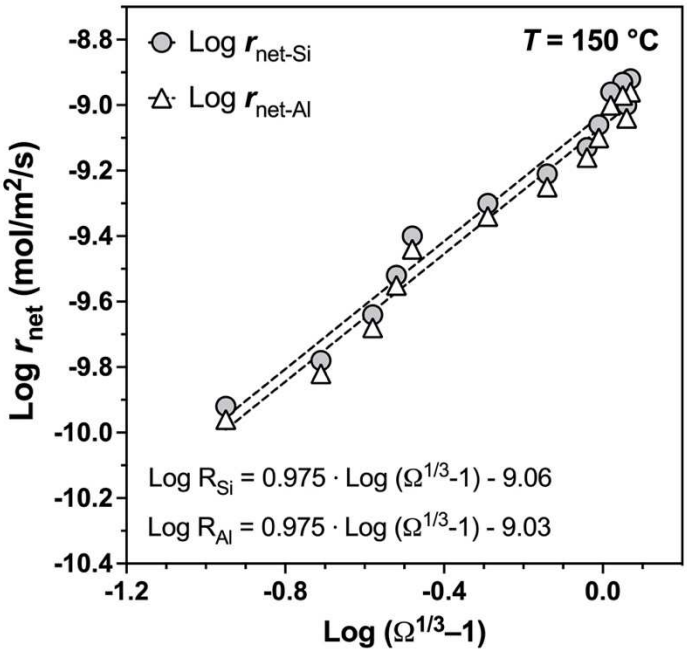

Fig. 8. Logarithmic plot of net rates calculated at 150°C against the corresponding degree of saturation of the aqueous solution ($\Omega^{1/3} - 1$). The dashed lines represent the least square fits of experimental data providing the rate constant of the dissolution/precipitation reaction.

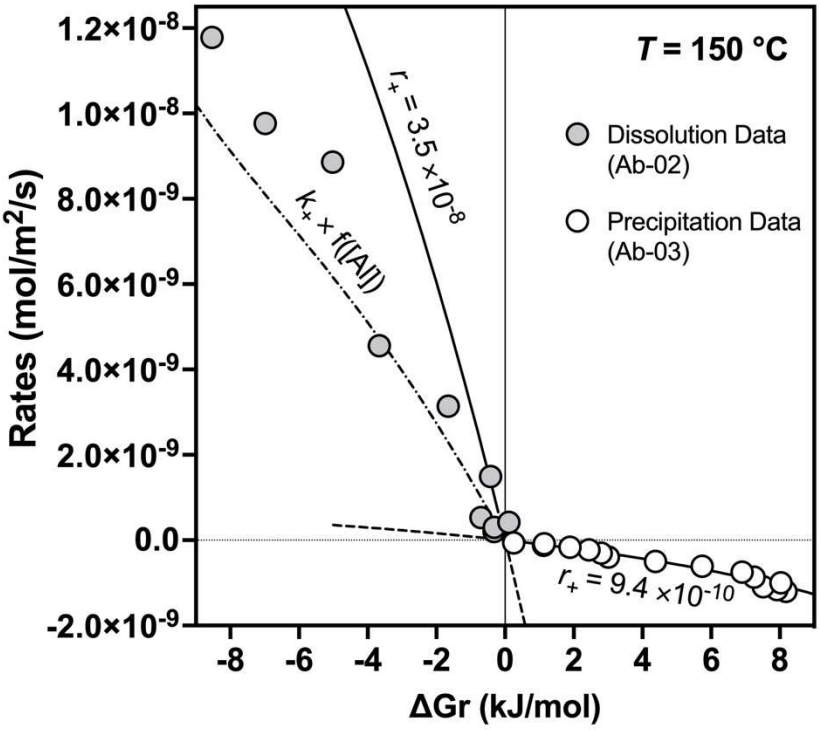

Fig. 9. Albite dissolution and precipitation rates as a function of the free energy change for the reaction at 150°C and pH = 9. The symbols stand for the experimental data, whereas the lines represent fits of the data to Eqs. (5-6), including also the inhibiting effect of dissolved Al on dissolution (dashed-dotted line, see text for details). Albite precipitation rates were determined by the relaxation technique (albite dissolution at 180°C until achievement of equilibrium followed by a temperature jump to 150°C). The values of albite dissolution rate constants k_+ corresponding to Eqs. (4-5) are equal to 3.5×10^{-8} mol.m^{-2}.s^{-1} (dissolution) and 9.4×10^{-10} mol.m^{-2}.s^{-1} (precipitation).

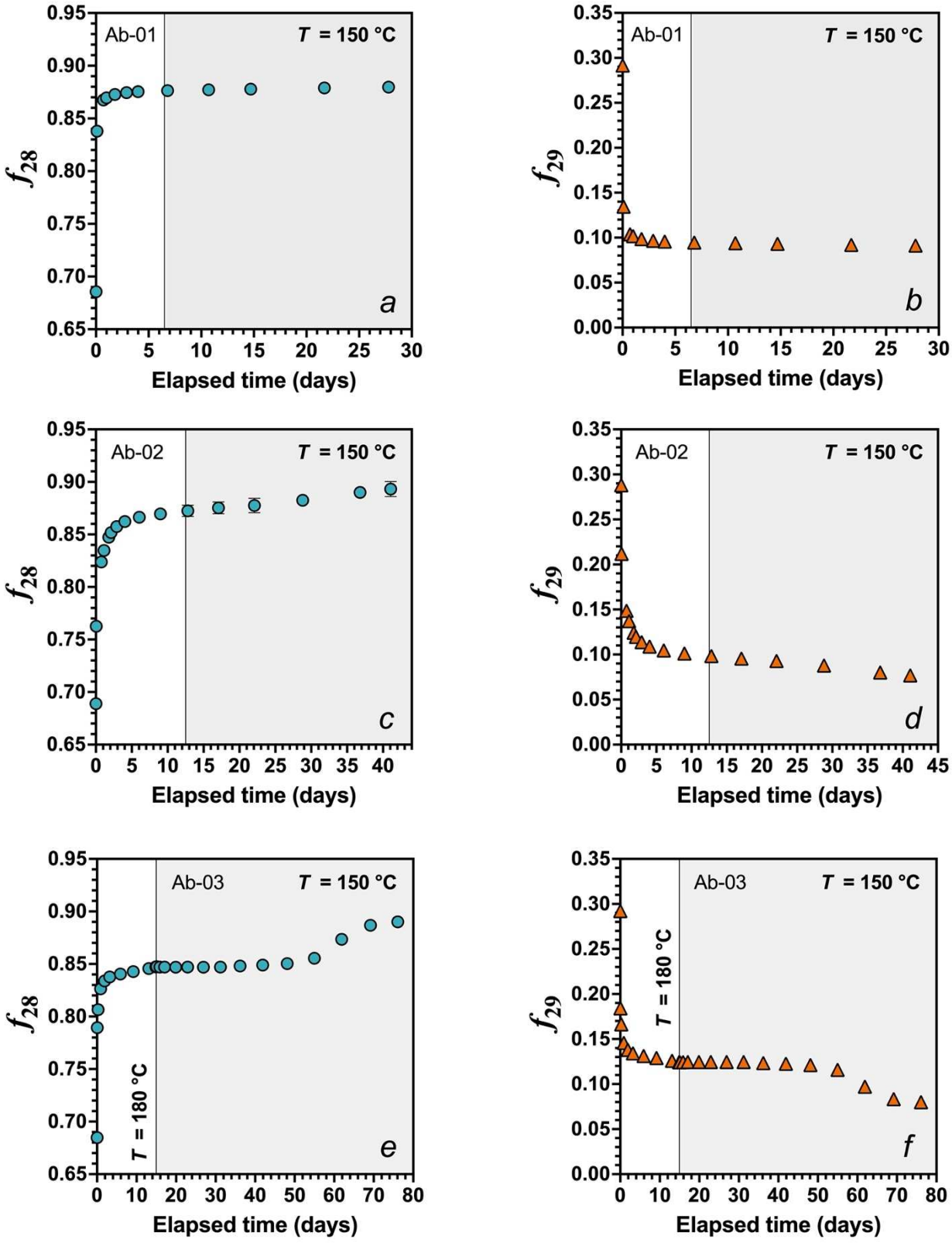

Fig. 10. Evolution of Si isotope fractional abundances (f_{28}, f_{29}) during the three batch experiments conducted in this study. The shaded regions of the plot areas for experiments Ab-01 and Ab-02 (a-d) define the steady-state conditions, where the concentrations of the dissolved constituents (Si, Al and Na) were constant over time. The shaded area on the plots for experiment Ab-03 identifies the part of the experiment conducted at different temperature (150 °C), where the precipitation reaction was initiated.

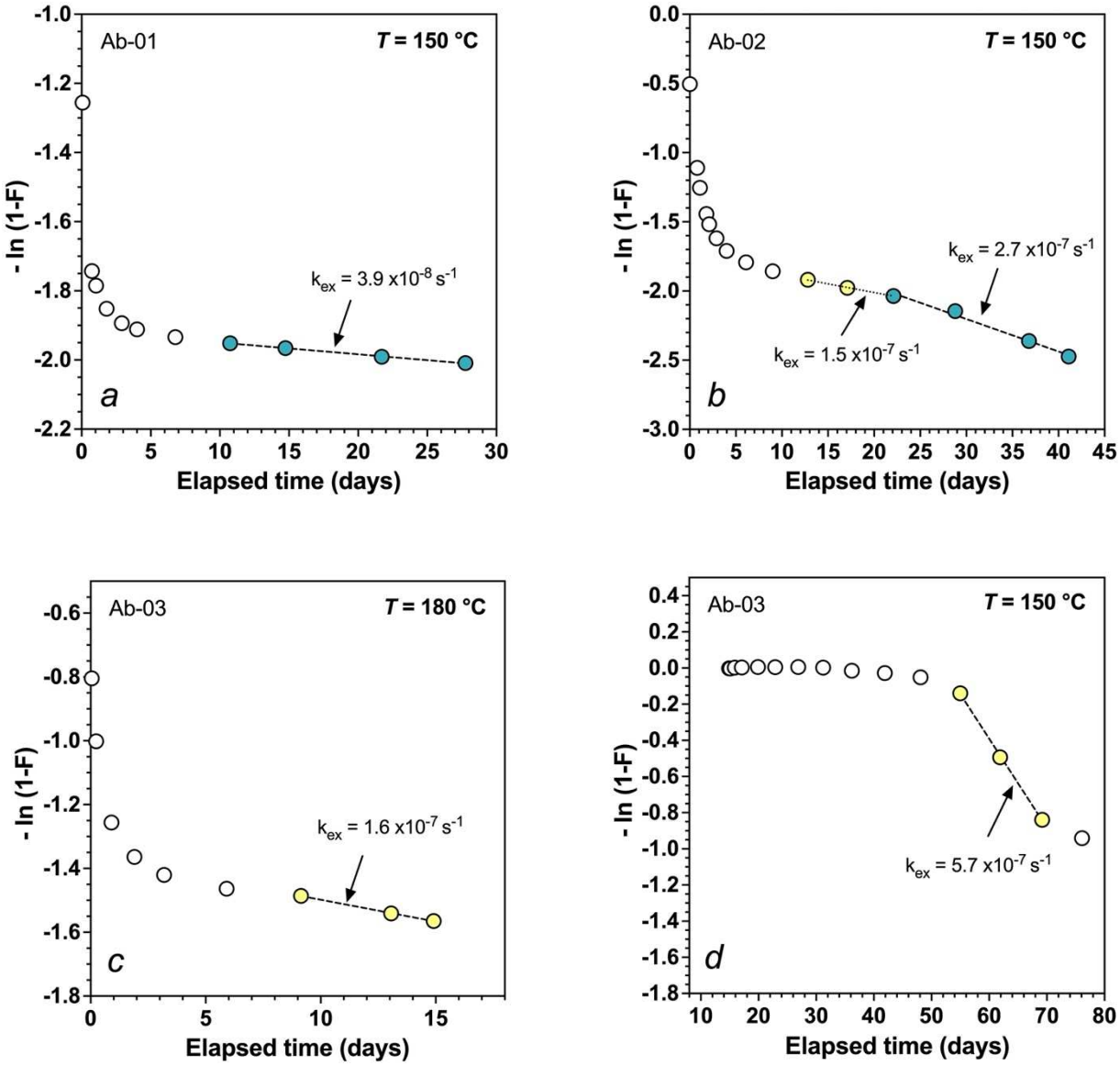

Fig. 11. Temporal evolution of the extent of isotope exchange (F) towards equilibrium during albite dissolution and precipitation for the three batch experiments conducted in this study. Rate constants of isotopic exchange (k_{ex}) at chemical steady state are derived by linear interpolation of F values (1st order rate law) as indicated on the plots by the straight lines drawn through the colored symbols. The corresponding isotope exchange constants referred to the albite surface area present in the system are provided in in Tables A1-A3.

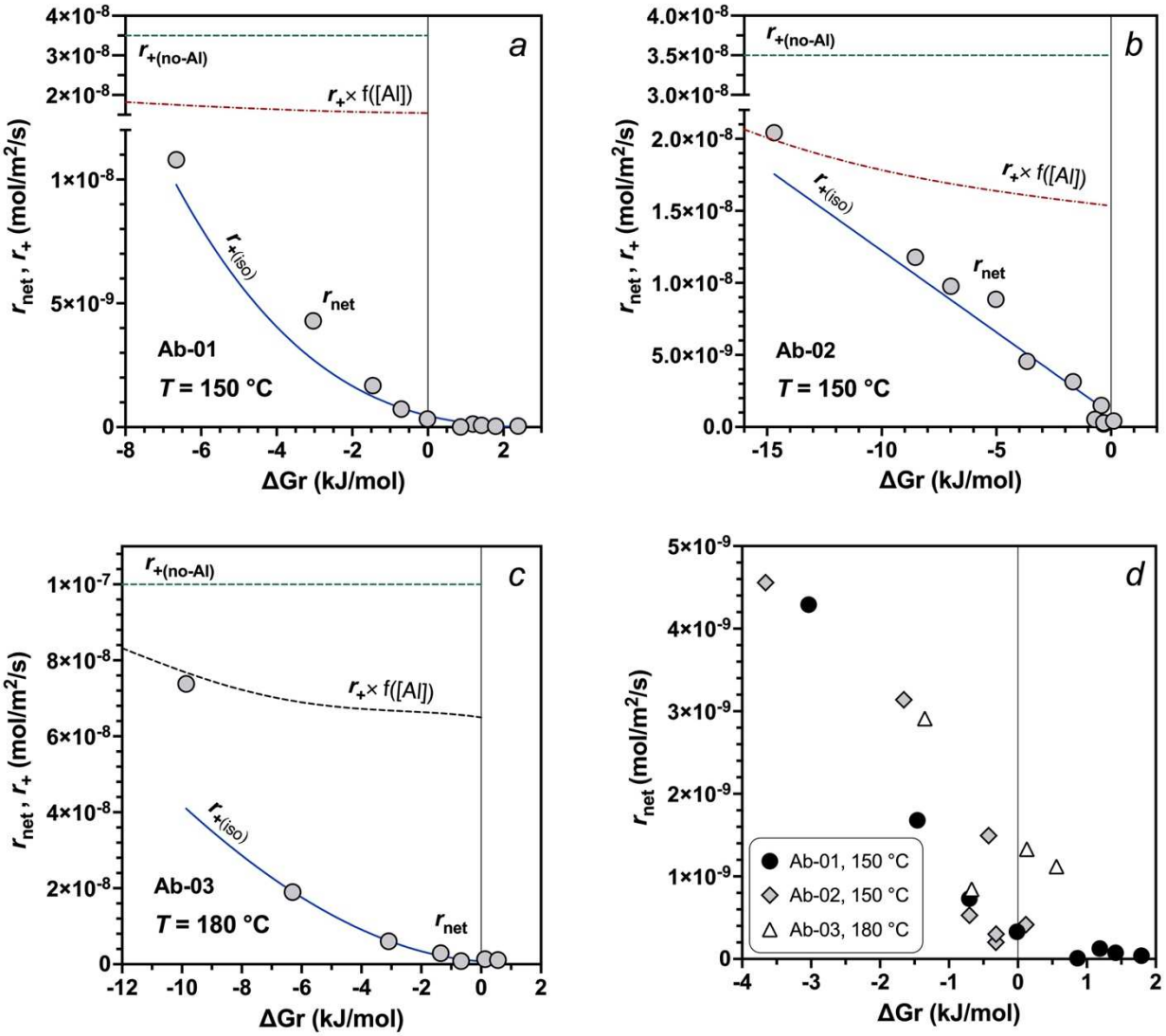

Fig. 12. Comparison of the rates of albite dissolution (r_{net}) measured during the batch experiments Ab-01 (a), Ab-02 (b) and Ab-03 (c) with the corresponding forward rate (r_+) models determined by analysis of chemical and isotopic data as a function of the Gibbs free energy of the reaction. Grey circles represent the rate measurements derived from Si concentration changes (r_{net}); the green dashed line is the value of the forward rate constant not including the effect of dissolved Al on the rates ($r_{+(no\text{-}Al)}$); the red dashed-dotted line describes the forward rate including the Al inhibitory term ($r_+ \times f([Al])$); the two blue solid lines illustrate the distributions of the forward rate values determined by modelling of Si isotope data ($r_{+(iso)}$). Note that the solid lines are non-linear (a) and linear (b) fits of the calculated r_+ values showing that, as equilibrium with respect to albite is approached, backward rates (r_-) remain negligible compared to the forward rates, $r_{+(iso)}$ being very close to the net rates of albite dissolution (see Table 8). The plot in (d) is a close-up view of the r_{net} values of the three experiments in the near-equilibrium region.

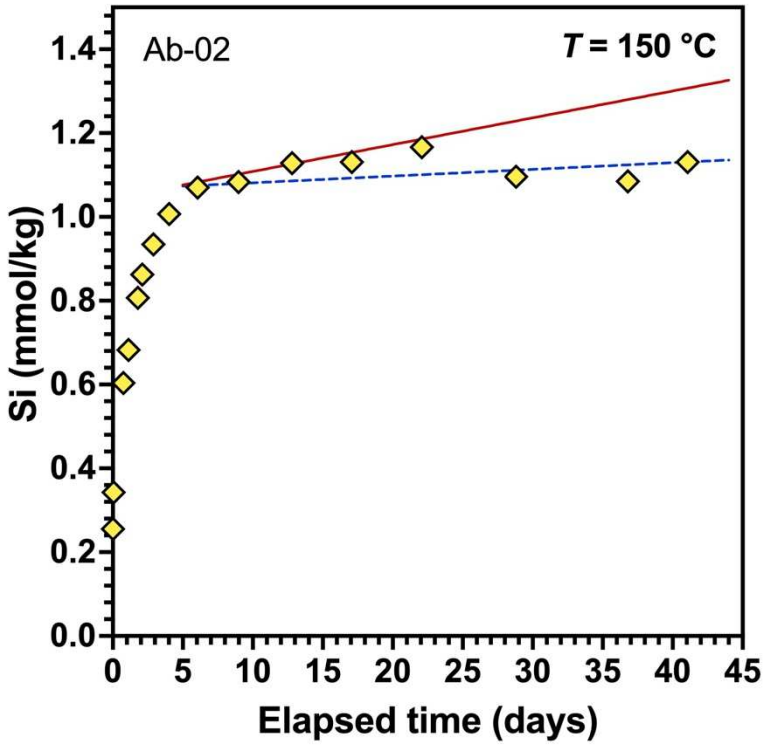

Fig. 13. Evolution of measured Si concentrations (symbols) during the batch experiment Ab-02 (pH 9, 150 °C) and predictions made by Eq. (13) using albite reaction rates derived from the analyses of Si isotope fractional abundances (f_{28}, f_{29}). The red solid line represents the Si concentrations obtained assuming no backward reaction ($r'_{-} = 0$), whereas the blue dashed line represent the Si concentrations calculated using the precipitation rate values obtained by fitting the experimental data according to Eq. (13).

Table 1. Summary of the starting conditions of the albite batch equilibration experiments conducted in the present study and albite Si isotope composition.

Expt. #	**Temp.** (°C)	**Albite** (g)	**Solution** (g)	**pH (25 °C)**	**Na** mM	**Si** mM	f_{28}	f_{29}	f_{30}
Ab-01	150	0.6403	426.0	11.63	4.69	0.259	0.6857	0.2916	0.0227
Ab-02	150	0.2143	427.1	11.63	4.75	0.255	0.6889	0.2879	0.0231
Ab-03	180/150	0.2151	408.8	11.62	4.40	0.622	0.6848	0.2921	0.0231
Albite sample							0.9223	0.0467	0.031

Table 2. List of the albite dissolution experiments conducted with a 300 ml mixed-flow reactor at 150 °C and their starting conditions. *d* stands for the fluid flow rate through the reactor.

Expt. #	**Albite mass**	**pH**	**NaOH**	**Si**	**Al**	***d***	**Duration**
	g	(25 °C)	mM	mM	mM	g/min	hrs
Ab-04	0.117	11.39	3.66	0	0	2.8	24.3
Ab-05	0.7207	11.41	3.73	0	0	2.5	26.3
Ab-06	0.1241	11.62	3.77	0	0	8.3	8.0

Table 3. List of symbols and definitions

Symbol	Definition
A	Chemical affinity of a given reaction, A = - □Gr (kJ mol^{-1})
ΔG_r	Gibbs free energy of a given reaction (kJ mol^{-1})
ΔG_f^o	The standard Gibbs free energy of formation (kJ mol^{-1})
ΔH^o_T	The standard enthalpy of reaction at temperature T (kJ mol^{-1})
K_{sp}	Solubility product
IAP	Ionic activity product
Ω	Solution saturation state with respect to a solid, □ = IAP/K_{sp}
F	$F = \frac{^{29/28}Si(t) - ^{29/28}Si(0)}{^{29/28}Si(eq) - ^{29/28}Si(0)}$ fraction of Si isotopic exchange
f_{28}	^{28}Si fractional abundance (0 to 1) in experimental solution $f_{28} = [^{28}Si]/([^{28}Si] + [^{29}Si] + [^{30}Si])$; $f_{28} = \frac{1}{1+R_{29/28}+R_{30/28}}$; $R_{29/28}$ stands for the isotopic ratio; similarly for f_{29} and f_{30}
k_+	Forward rate constant of albite dissolution in mol (albite) m^{-2} s^{-1}
k_-	Backward rate constant of albite dissolution in mol (albite) m^{-2} s^{-1}
k_{ex}	Rate constant of isotope exchange in mol. m^{-2} s^{-1}
R	Gas constant (8.314 J mol^{-1} K^{-1})
r_{net}	Net or overall reaction rate in mol (albite) m^{-2} s^{-1}; $r_{net} = r_+ - r_-$
r_+	Forward rate of feldspar dissolution in mol (feldspar) m^{-2} s^{-1}
r'_+	Forward rate of albite dissolution in mol (feldspar) L^{-1} s^{-1}; $r'_+ = r_+ \cdot S_A$
r_-	Reverse rate of albite dissolution reaction (precipitation or formation) in mol (albite) m^{-2} s^{-1}; similarly, for r'_-
v	stoichiometric coefficient in the mineral formula of albite
S_A	Surface area load of feldspar (m^2/L) in the reactor; S_A=s_A*m/V, where m denotes the mass (g) of reactant, V the volume of solution in the reactor, and s_A the specific BET surface area (m^2/g). e.g., 0.136m^2/g*1.0g/0.01L for albite

Table 4. Fluid chemical evolution and calculated rates of albite dissolution during the batch experiment Ab-01 (pH 9, 150 °C). See Table 2 for the starting conditions.

Sample	time	pH	pH	Na	Si	Al	ΔSi/ΔAl	Log IAP	ΔGr	Rates (Si)
	days	(25°C)	(150°C)	mM	mM	mM			kJ/mol	mol/m^2/s
Ab1-00	0.0	11.63	9.22	4.68	0.26	0.00		-	-	-
Ab1-01	0.1	11.48	9.09	4.80	0.67	0.10	4.2	-17.4	-17.6	1.17×10^{-7}
Ab1-02	0.7	-	9.11	4.97	1.07	0.26	2.5	-16.4	-6.7	1.08×10^{-8}
Ab1-03	1.0	11.50	9.13	5.03	1.13	0.28	2.5	-16.3	-3.0	4.29×10^{-9}
Ab1-04	1.8	11.46	9.10	5.06	1.21	0.31	2.4	-16.1	-1.5	1.68×10^{-9}
Ab1-05	2.9	-	9.10	5.04	1.25	0.33	2.7	-16.1	-0.7	7.31×10^{-10}
Ab1-06	4.0	11.44	9.08	5.10	1.28	0.34	3.8	-16.0	0.0	3.30×10^{-10}
Ab1-07	6.8	11.37	9.03	5.31	1.30	0.34	4.1	-15.8	1.2	1.26×10^{-10}
Ab1-08	10.7	11.37	9.03	5.15	1.32	0.35	2.3	-15.8	1.4	7.59×10^{-11}
Ab1-09	14.7	11.35	9.01	5.12	1.33	0.36	1.7	-15.8	1.8	3.90×10^{-11}
Ab1-10	21.7	11.43	9.07	5.13	1.33	0.36	1.1	-15.9	0.9	8.99×10^{-12}
Ab1-11	27.8	11.32	8.99	5.17	1.35	0.37	2.6	-15.7	2.4	4.46×10^{-11}

Table 5. Fluid chemical evolution and calculated rates of albite dissolution during the batch experiment Ab-02 (pH 9, 150 °C). See Table 2 for the starting conditions.

Sample	**time**	**pH**	**pH**	**Na**	**Si**	**Al**	**ΔSi/ΔAl**	**Log IAP**	**ΔGr**	**Rates (Si)**
	days	(25°C)	(150°C)	mM	mM	mM			kJ/mol	mol/m^2/s
Ab2-00	0.0	11.63	9.22	4.75	0.26	0.00	-	-	-	-
Ab2-01	0.0	11.49	9.09	4.78	0.34	0.04	2.1	-18.6	-23.7	1.02×10^{-7}
Ab2-02	0.8	11.58	9.18	4.97	0.60	0.16	2.1	-17.5	-14.7	2.04×10^{-8}
Ab2-03	1.1	11.52	9.13	4.97	0.68	0.20	2.4	-17.1	-8.5	1.18×10^{-8}
Ab2-04	1.8	11.56	9.17	5.01	0.81	0.24	2.7	-16.9	-7.0	9.77×10^{-9}
Ab2-05	2.1	11.54	9.15	5.04	0.86	0.26	3.4	-16.8	-5.0	8.86×10^{-9}
Ab2-06	2.9	11.52	9.14	5.07	0.93	0.29	2.6	-16.6	-3.7	4.56×10^{-9}
Ab2-07	4.0	11.46	9.09	5.12	1.01	0.31	3.0	-16.3	-1.7	3.14×10^{-9}
Ab2-08	6.1	11.44	9.07	5.13	1.07	0.33	3.0	-16.2	-0.4	1.49×10^{-9}
Ab2-09	9.0	11.47	9.10	5.15	1.08	0.34	1.3	-16.2	-0.3	2.03×10^{-10}
Ab2-10	12.8	11.52	9.14	5.23	1.13	0.35	12.9	-16.3	-0.7	5.30×10^{-10}
Ab2-11	17.1	11.45	9.08	5.25	1.13	0.34	-0.5	-16.1	*0.5*	2.40×10^{-11}
Ab2-12	22.1	11.52	9.14	5.23	1.17	0.35	7.5	-16.2	-0.3	3.02×10^{-10}
Ab2-13	28.8	11.58	9.19	5.39	1.10	0.28	1.1	-16.5	*-1.7*	-4.27×10^{-10}
Ab2-14	36.8	11.57	9.19	5.33	1.08	0.25	0.4	-16.5	*-2.5*	-5.68×10^{-11}
Ab2-15	41.1	11.39	9.03	5.34	1.13	0.25	13.6	-16.2	0.1	4.15×10^{-10}

Table 6. Fluid chemical evolution and calculated rates of albite dissolution/precipitation during the batch experiment Ab-03 (pH 9, 180 & 150°C). See Table 2 for the starting conditions. Note that the ΔG_r values and Rates relative to the second part of the experiment (150 °C) refer to the fit of the relaxation equation to the experimental data for the corresponding time.

	Sample	**time**	**pH**	**pH**	**Na**	**Si**	**Al**	**ΔSi/ΔAl**	**Log IAP**	**ΔGr**	**Rates (Si)**
		days	(25°C)	(T)	mM	mM	mM			kJ/mol	mol/m^2/s
180 °C	Ab3-00	0.0	11.62	9.00	4.40	0.62	0.00	-	-	-	-
	Ab3-01	0.0	11.31	8.87	4.32	0.97	0.08	4.4	-16.5	-18.3	3.85×10^{-7}
	Ab3-02	0.2	11.49	8.83	4.52	1.23	0.16	3.2	-16.1	-9.9	7.38×10^{-8}
	Ab3-03	0.9	11.45	8.89	4.65	1.48	0.26	2.5	-15.6	-6.3	1.90×10^{-8}
	Ab3-04	1.9	11.37	8.86	4.69	1.60	0.31	2.5	-15.4	-3.1	6.06×10^{-9}
	Ab3-05	3.2	11.33	8.82	4.73	1.67	0.33	3.2	-15.2	-1.3	2.91×10^{-9}
	Ab3-06	5.9	11.35	8.82	4.77	1.72	0.34	6.1	-15.2	-0.7	8.43×10^{-10}
	Ab3-07	9.1	11.33	8.82	4.66	1.70	0.34	30.4	-15.2	-0.6	-3.93×10^{-10}
	Ab3-08	13.1	11.25	8.79	4.65	1.81	0.35	14.9	-15.1	0.1	1.33×10^{-9}
	Ab3-09	14.9	11.26	8.77	4.41	1.86	0.31	-1.1	-15.1	0.6	1.12×10^{-9}
150 °C	Ab3-10	14.9	-	8.77	4.41	1.83	0.30	2.5	-15.3	8.18	-1.20×10^{-9}
	Ab3-11	15.1	11.28	8.98	4.69	1.78	0.34	-1.2	-15.3	7.92	-1.16×10^{-9}
	Ab3-12	15.9	11.3	8.99	4.48	1.80	0.34	-5.2	-15.4	7.52	-1.09×10^{-9}
	Ab3-13	17.1	11.22	8.97	4.67	1.85	0.31	-1.5	-15.3	8.03	-1.00×10^{-9}
	Ab3-14	19.9	11.24	8.95	4.57	1.80	0.32	-3.0	-15.4	7.25	-8.69×10^{-10}
	Ab3-15	22.9	11.21	8.95	4.49	1.77	0.30	1.7	-15.5	6.90	-7.47×10^{-10}
	Ab3-16	26.9	11.25	8.95	4.42	1.71	0.28	2.9	-15.6	5.74	-6.13×10^{-10}
	Ab3-17	31.2	11.31	8.98	4.38	1.55	0.25	4.2	-15.8	4.38	-5.00×10^{-10}
	Ab3-18	36.2	11.37	8.99	4.47	1.54	0.19	0.1	-15.9	3.01	-3.96×10^{-10}
	Ab3-19	41.9	11.33	9.02	4.53	1.56	0.22	0.5	-16.0	2.80	-3.04×10^{-10}
	Ab3-20	48.1	11.29	8.99	4.45	1.53	0.21	1.9	-16.0	2.44	-2.29×10^{-10}
	Ab3-21	55.0	11.28	8.98	4.39	1.43	0.18	3.4	-16.1	1.89	-1.67×10^{-10}
	Ab3-22	61.9	11.27	8.96	3.69	1.20	0.12	3.8	-16.2	1.12	-1.21×10^{-10}
	Ab3-23	69.2	11.19	8.92	3.23	1.19	0.16	-0.2	-16.2	1.14	-8.63×10^{-11}
	Ab3-24	76.1	11.23	8.90	3.03	1.17	0.15	4.3	-16.3	0.25	-6.24×10^{-11}

Table 7. Results of the albite dissolution experiments conducted at 150 °C and at far-from-equilibrium conditions using a mixed-flow Ti-reactor. Reported element concentrations refer to steady-state conditions. Note that the dissolution rates are normalized to the initial BET specific surface area.

Expt. #	**pH** (150°C)	**Na** mM	**Al** mM	**Si** mM	**ΔSi/ΔAl**	**ΔGr** kJ/mol	**Rates (Al)** $mol.m^{-2}.s^{-1}$	**Rates (Si)** $mol.m^{-2}.s^{-1}$
Ab-04	8.97	3.67	1.68E-02	4.19E-02	2.5	-45.1	4.88×10^{-8}	4.06×10^{-8}
Ab-05	9.00	3.79	5.68E-02	1.46E-01	2.6	-27.8	2.40×10^{-8}	2.05×10^{-8}
Ab-06	9.08	3.75	4.90E-03	1.18E-02	2.4	-63.8	4.04×10^{-8}	3.07×10^{-8}

Table 8. Summary of the forward rate (r_+) and rate constant (k_+) values for the albite dissolution/precipitation reaction as determined (i) by the measured changes of Si concentration (Δ[Si]) according to the TST, Eqs. (4-6) and (ii) by analysis of Si isotopes (f_{28}-f_{29}) at pH 9 and 150 and 180 °C for the batch experiments carried out in this study. The table reports the reaction times and the Gibbs free energy of albite dissolution (ΔG_r) as a function of which the rate values were determined.

Temp.	Expt. #	r_+	k_+	time span	ΔGr	Rate source	R^2	Model type
°C		mol.m^{-2}.s^{-1}	mol.m^{-2}.s^{-1}	days	kJ/mol			
150	All expts.	3.5×10^{-8}	-	0-41.1	-64 to 0	Δ[Si]	0.884	TST- r_+
	All expts	-	3.5×10^{-8}	0-41.1	-64 to 0	Δ[Si]	0.926	TST-k_+ w/Al
	Ab-01	1.0×10^{-10}	-	0-27.8	-17.6 to 2.4	f_{28}-f_{29}	0.968	single r_+
	Ab-01	1.3×10^{-7}	-	0.1	-17.6	f_{28}-f_{29}	1	variable r_+
		9.8×10^{-9}	-	0.7	-6.7			
		2.5×10^{-9}	-	1.0	-3.0			
		1.7×10^{-9}	-	1.8	-1.5			
		7.4×10^{-10}	-	2.9	-0.7			
		3.3×10^{-10}	-	4.0	0.0			
		1.7×10^{-10}	-	6.8	1.2			
		9.2×10^{-11}	-	10.7	1.4			
		7.5×10^{-11}	-	14.7	1.8			
		7.4×10^{-11}	-	21.7	0.9			
		6.0×10^{-11}	-	27.8	2.4			
	Ab-02	5.0×10^{-10}	-	0-41.1	-23.7 to 0.1	f_{28}-f_{29}	0.963	single r_+
	Ab-02	1.4×10^{-7}	-	0.0	-23.7	f_{28}-f_{29}	1	variable r_+
		1.7×10^{-8}	-	0.8	-14.7			
		1.1×10^{-8}	-	1.1	-8.5			
		9.0×10^{-9}	-	1.8	-7.0			
		8.1×10^{-9}	-	2.1	-5.0			
		4.8×10^{-9}	-	2.9	-3.7			
		3.2×10^{-9}	-	4.0	-1.7			
		1.7×10^{-9}	-	6.1	-0.4			
		1.1×10^{-9}	-	9.0	-0.3			
		7.1×10^{-10}	-	12.8	-0.7			
		6.7×10^{-10}	-	17.1	0.5			
		5.3×10^{-10}	-	22.1	-0.3			
		8.6×10^{-10}	-	28.8	-1.7			
		1.3×10^{-9}	-	36.8	-2.5			
		1.1×10^{-9}	-	41.1	0.1			
	Ab-03	9.4×10^{-10}	-	14.9-76.1	0 to 8.2	Δ[Si]	0.970	TST- r_+
	Ab-03	5.0×10^{-10}	-	14.9-76.1	0 to 8.2	f_{28}-f_{29}	0.932	single r_+
	Ab-03	$< 1\times10^{-11}$	-	14.9	8.2	f_{28}-f_{29}	1	variable r_+
		$< 1\times10^{-11}$	-	15.1	7.9			
		$< 1\times10^{-11}$	-	15.9	7.5			
		$< 1\times10^{-11}$	-	17.1	8.0			
		$< 1\times10^{-11}$	-	19.9	7.2			
		$< 1\times10^{-11}$	-	22.9	6.9			
		$< 1\times10^{-11}$	-	26.9	5.7			
		2.7×10^{-11}	-	31.2	4.4			
		1.4×10^{-10}	-	36.2	3.0			
		8.7×10^{-11}	-	41.9	2.8			
		1.3×10^{-10}	-	48.1	2.4			
		4.4×10^{-10}	-	55.0	1.9			

Temp.	Expt. #	r_+	k_+	time span	ΔGr	Rate source	R^2	Model type
°C		mol.m^{-2}.s^{-1}	mol.m^{-2}.s^{-1}	days	kJ/mol			
		1.9×10^{-9}	-	61.9	1.1			
		1.7×10^{-9}	-	69.2	1.1			
		4.5×10^{-10}	-	76.1	0.2			
180	Ab-03	1.0×10^{-7}	-	0-14.9	-9.9 to 0	Δ[Si]	0.690	TST- r_+
	Ab-03	-	1.0×10^{-7}	0-14.9	-9.9 to 0	Δ[Si]	0.812	TST- k_+ w/Al
	Ab-03	1.5×10^{-9}	-	0-14.9	-9.9 to 0	f_{28}-f_{29}	0.906	single r_+
	Ab-03	5.4×10^{-7}	-	0.0	-18.3	f_{28}-f_{29}	1	variable r_+
		4.1×10^{-8}	-	0.2	-9.9			
		1.9×10^{-8}	-	0.9	-6.3			
		6.3×10^{-9}	-	1.9	-3.1			
		2.7×10^{-9}	-	3.2	-1.3			
		1.0×10^{-9}	-	5.9	-0.7			
		6.7×10^{-10}	-	9.1	-0.6			
		7.7×10^{-10}	-	13.1	0.1			
		8.4×10^{-10}	-	14.9	0.6			